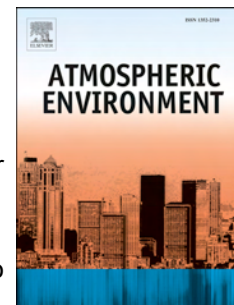


Accepted Manuscript

Episode study of fine particle and ozone during the CAPUM-YRD over Yangtze River Delta of China: characteristics and source attribution

Lei Shu, Tijian Wang, Min Xie, Mengmeng Li, Ming Zhao, Ming Zhang, Xiuyong Zhao



PII: S1352-2310(19)30074-3

DOI: <https://doi.org/10.1016/j.atmosenv.2019.01.044>

Reference: AEA 16533

To appear in: *Atmospheric Environment*

Received Date: 17 July 2018

Revised Date: 15 January 2019

Accepted Date: 19 January 2019

Please cite this article as: Shu, L., Wang, T., Xie, M., Li, M., Zhao, M., Zhang, M., Zhao, X., Episode study of fine particle and ozone during the CAPUM-YRD over Yangtze River Delta of China: characteristics and source attribution, *Atmospheric Environment*, <https://doi.org/10.1016/j.atmosenv.2019.01.044>.

This is a PDF file of an unedited manuscript that has been accepted for publication. As a service to our customers we are providing this early version of the manuscript. The manuscript will undergo copyediting, typesetting, and review of the resulting proof before it is published in its final form. Please note that during the production process errors may be discovered which could affect the content, and all legal disclaimers that apply to the journal pertain.

Episode study of fine particle and ozone during the CAPUM-YRD over Yangtze River Delta of China: characteristics and source attribution

Lei Shu^a, Tijian Wang^{a,*}, Min Xie^a, Mengmeng Li^a, Ming Zhao^a, Ming Zhang^b, Xiuyong

5 Zhao^b

^a School of Atmospheric Sciences, Nanjing University, Nanjing 210023, China

^b State Environmental Protection Key Laboratory of Atmospheric Physical Modeling and Pollution Control, Nanjing 210023, China

10 *Correspondence: Tijian Wang (tjwang@nju.edu.cn)

Abstract

Fine particle ($PM_{2.5}$) and ozone (O_3) are major air pollutants in China, especially in developed city clusters. A comprehensive field campaign, the Campaign on Air Pollution and Urban Meteorology

15 in Yangtze River Delta (CAPUM-YRD), eastern China is carried out in 2016 to enhance the understanding of regional $PM_{2.5}$ and O_3 pollution. Two super sites in Shanghai, one in Hangzhou, as well as nineteen national monitoring stations in Nanjing and Hefei jointly participate in the campaign. In this study, regional $PM_{2.5}$ and O_3 pollution episodes are characterized based on summer and winter experiments during the CAPUM-YRD. Further, trajectory simulation and

20 source apportionment technology in Comprehensive Air Quality Model with extensions (CAMx) are applied to reveal the source of the pollution episodes. We find regional synchronous $PM_{2.5}$ pollution episodes (over $120 \mu g/m^3$) occur frequently throughout YRD. Secondary inorganic and

carbonaceous components account for a major proportion (70-80%) in $PM_{2.5}$. Nitrate concentration is significantly higher (lower) than sulfate in winter (summer). The secondary

25 conversion of sulfur and nitrogen increases alongside elevated $PM_{2.5}$ levels, with a maximum ratio of 0.28 and 0.17 in winter, respectively. Source apportionment results suggest that the contribution

of emissions within YRD dominates in $PM_{2.5}$ (over 60%) compared to other regions. The inter-regional transport from the north-northwest can contribute over 20% to $PM_{2.5}$ in YRD, with a maximum of 28.4% in Nanjing. Under the transport by enhanced northerly winds, $PM_{2.5}$

30 concentrations may increase explosively, with an observation evidence of peak values in Hefei

(312.6 $\mu\text{g}/\text{m}^3$) and Nanjing (255.7 $\mu\text{g}/\text{m}^3$). Moreover, high levels and remarkable spatial heterogeneity of surface O_3 are observed over YRD in summer, with daily maximum 8-hour average O_3 above 300 $\mu\text{g}/\text{m}^3$ in Nanjing. The occurrence of O_3 pollution episodes is significantly impacted by favorable stagnant weather conditions and transport at multiple spatial scales.

35 Regional contribution results demonstrate that super-regional transport is prominent (29.4-50.7%) in O_3 , especially in coastal cities like Shanghai (30.3-63.0%). Our results suggest that enhanced regional collaboration and efforts are of extreme necessity in long-term and optimized control of severe $\text{PM}_{2.5}$ and O_3 pollution in YRD.

40 **Keywords:** $\text{PM}_{2.5}$; O_3 ; regional transport; source apportionment; Yangtze River Delta

1. Introduction

China has experienced increasingly serious air pollution over the last decade as the economy develops rapidly. According to the official statistics (<http://www.mee.gov.cn/>), fine particle ($\text{PM}_{2.5}$) and ozone (O_3) are frequently reported as the primary pollutant, leading to adverse impacts on public health and vegetation growth (Seaton et al., 1995; Chan and Yao et al., 2008; Kan et al., 2012). Nowadays, severe $\text{PM}_{2.5}$ and O_3 pollution has become an important issue in China, especially in the developed megacity clusters, such as the Beijing-Tianjin-Hebei (BTH) region (Wang et al., 2005, 2014, 2017; Zheng et al., 2015; Hu et al., 2014), the Yangtze River Delta (YRD) region (Li et al., 2011, 2015b, 2016; Ding et al., 2013; Ming et al., 2017; Xie et al., 2014, 2016; Shu et al., 2016, 2017) and the Pearl River Delta region (Wang et al., 2006; Li et al., 2012; Wu et al., 2013a, b). The Chinese government and the public have made great efforts to combat the air pollution since the Air Pollution Prevention and Control Action Plan is promulgated in 2013, achieving obvious improvement in air quality (Zhang et al., 2016; Feng and Liao, 2016; Cai et al., 2017). However, despite the remarkable decrease in $\text{PM}_{2.5}$ levels, it is still a challenge to meet the National Ambient Air Quality Standards (NAAQS) (35 $\mu\text{g}/\text{m}^3$ for annual average $\text{PM}_{2.5}$) for megacity clusters. Besides, extremely high O_3 levels occur frequently in recent years (Wang et

al., 2017; Li et al., 2016; Xie et al., 2016). The chemical transformation, the effect of meteorology and policy-relevant questions make the prevention and control of regional PM_{2.5} and O₃ pollution
60 quite complicated.

As one of the typical polluted regions, YRD is located in the southeast coastal area of eastern China, featuring subtropical monsoon climate. It is one of the most developed urban economic circles in China, including part of Jiangsu, Zhejiang and Anhui provinces and Shanghai municipality. Over the past few years, regional severe PM_{2.5} and O₃ pollution episodes become
65 quite common and have been investigated by many studies (Li et al., 2011, 2015b, 2016; Fu et al., 2016; Hua et al., 2015; Ding et al., 2013; Hu et al., 2014; Jiang et al., 2012; Gao et al., 2016; Shi et al., 2015; Xie et al., 2016; Shu et al., 2016, 2017; Ming et al., 2017; Pu et al., 2017). It is found that the heavy particle loading is commonly observed in winter over YRD, while the transport of massive pollutants from northern China can easily aggravate the pollution in YRD (Li et al., 2011;
70 Fu et al., 2016; Ming et al., 2017). Organic matter and secondary inorganic ions usually account for substantial proportions in PM_{2.5} in polluted days (Hua et al., 2015; Ming et al., 2017; Qiao et al., 2018). The formation of O₃ is mostly under VOC-limited situation in YRD, implying that VOC emissions should be controlled in priority (Wang et al., 2017; Ding et al., 2013; Li et al., 2016; Xie et al., 2016). Besides, the relatively long atmospheric lifetime of O₃ favors the
75 long-range transport, which further increases the complexity of the evolution and persistence of photochemical pollution episodes, as well as the difficulty of O₃ control (Jiang et al., 2012; Ding et al., 2013; Han et al., 2018). Previous studies mostly focus on only one kind of air pollutant (PM_{2.5} or O₃). Therefore, an integrated analysis to improve the understanding of the formation process (including transport characteristics and source attribution) of these two air pollutants in
80 YRD is desired.

Observation analysis and model simulations have been successfully implemented in studies regarding the features, causes, potential source and control measures of regional PM_{2.5} and O₃ pollution (Liu et al., 2010a, b; Li et al., 2011, 2015b, 2016; Wu et al., 2013a; Gao et al., 2016). Numerical models are convinced to be an effective tool to show the three-dimensional
85 temporal-spatial distribution of air pollution, and further reveal potential formation mechanisms

with no limitation on the number and position of monitoring sites. However, model simulations have significant uncertainties resulting from multiple reasons, such as model algorithm, spatiotemporal resolution and emission inventory etc. Therefore, comprehensive stereoscopic observation programs play a critical role in better understanding the regional air pollution, helping 90 to make optimized abatement measures of emissions (Vautard et al., 2003; Zhang et al., 2008). Nevertheless, this kind of regional observational campaign is still quite limited to YRD. A comprehensive observational stereoscopic campaign is of great necessity and urgency to support integrated researches on regional PM_{2.5} and O₃ pollution over YRD.

In 2016, the Campaign on Air Pollution and Urban Meteorology in Yangtze River Delta 95 (CAPUM-YRD) is carried out to provide an in-depth understanding of multi-dimensional regional PM_{2.5} and O₃ pollution and associated urban meteorology in YRD. As part of the CAPUM-YRD, this study is designed to enhance the knowledge of spatiotemporal variations and formation mechanisms of regional PM_{2.5} and O₃ pollution at the surface layer. Observations from super-national monitoring sites, as well as an air quality model (CAMx) are used to fulfill our 100 purpose. Firstly, the characteristics of regional PM_{2.5} and O₃ pollution are analyzed through identified polluted and clean episodes. Further, trajectory analysis and source apportionment technology incorporated into CAMx model are applied to illustrate the relative importance of different source regions to PM_{2.5} and O₃ pollution in YRD. The following part of this paper is organized as follows. Section 2 describes the observations and models. The major characteristics 105 of PM_{2.5} and O₃ pollution over YRD are presented in Section 3. Section 4 examines the impacts of transport on PM_{2.5} and O₃ levels in YRD qualitatively and quantitatively. A brief summary is addressed in Section 5.

2. Data and methods

110 2.1 Field observations

In 2016, two intensive collaborated synchronous field experiments during the CAPUM-YRD (details presented in the supplementary) are performed, namely summer experiment (from 14th August to 15th September) and winter experiment (from 24th November to 23rd December).

Hourly monitored records of air pollutants are collected from three super monitoring sites and
 115 nineteen national monitoring sites in YRD (Figure 1 and Table S1). Three super monitoring sites
 are Pudong (PD), Dianshanlake (DSL) sites in Shanghai, and Zhaohui (ZH) site in Hangzhou.
 Nine national monitoring sites in Nanjing and ten sites in Hefei are also covered (Table S1).

Hourly data of six criteria pollutants ($\text{PM}_{2.5}$, PM_{10} , O_3 , NO_2 , SO_2 and CO) are available at all
 22 sites. In addition, an online analyzer for Monitoring of AeRosols and GAses (MARGA, model
 120 ADI 2080 Applikon Analytical B. V. Corp., the Netherlands) is used to measure mass
 concentrations of major water-soluble inorganic ions at one-hour resolution. Nitrate (NO_3^-), sulfate
 (SO_4^{2-}) and ammonium (NH_4^+) data are obtained from PD, DSL, ZH and Caochangmeng (CCM)
 sites. Besides, a thermal/ optical carbon analyzer (DRI Model 2001A, Desert Research Institute,
 United States) is used to analyze elemental carbon (EC) and organic carbon (OC) compositions in
 125 $\text{PM}_{2.5}$ masses at PD, DSL and CCM site. Owing to the instrument failure, EC and OC at CCM site
 during the summer experiment only cover the period from 1st to 15th September. The
 observational data at National monitoring sites are obtained from China National Environmental
 Monitoring Centre (CNEMC) network (<http://www.cnemc.cn/>). The sampling methods and the
 QA/QC procedures used at each site are in accordance with the Chinese national standard
 130 HJ/T193-2005 (State Environmental Protection Administration of China, 2006).

2.2 Meteorological and satellite data

Hourly surface meteorological data are available at Hangzhou weather station (120.1667°E ,
 30.2333°N) provided by the National Meteorological Information Center of China Meteorological
 135 Administration (NMICMA). The data include temperature (T), relative humidity (RH), wind
 speed (WS), wind direction (WD), net radiation and 1-h accumulated precipitation. In addition,
 National Centers for Environmental Prediction (NCEP) Final (FNL) operational global analysis
 data are applied in the analysis of meteorological field over YRD
 (https://rda.ucar.edu/datasets/ds083.2/). This product is prepared operationally on 1-degree by
 140 1-degree grids every six hours (00:00, 06:00, 12:00 and 18:00 UTC) from the Global Data
 Assimilation System (GDAS).

Moderate Resolution Imaging Spectroradiometer (MODIS) Active Fire Collection 6 MCD14ML product is used to show the hotspots distribution in transport paths of air parcels to YRD. MCD14ML is a global monthly fire location product, and available at MODIS Active fire 145 and Burned Area products website (<http://modis-fire.umd.edu>, last accessed on 25th September 2017). The product contains the geographic location, date, and some additional information for each fire pixel detected by the Terra and Aqua MODIS sensors on a monthly basis. It adopts a contextual algorithm and applies thresholds to the observed brightness temperature from MODIS middle-infrared and thermal infrared channels. The Collection 6 detection algorithm is improved 150 to address the limitations of false detections with previous Collection 5 fire product (Giglio et al., 2016; Fornacca et al., 2017). The fire pixel counts at greater than 50% confidence interval are used in this study.

2.3 HYSPLIT model

155 Air parcel backward trajectories are computed to identify the source regions of air masses and the transport paths using the Hybrid Single-Particle Lagrangian Integrated Trajectory (HYSPLIT) Model (Version 4). The model is developed by National Oceanic and Atmospheric Administration (NOAA) Air Resources Laboratory (ARL) (Draxler and Rolph, 2013; Rolph, 2013; Stein et al., 2015). It has been successfully implemented in numerous studies involving atmospheric transport 160 and dispersion modeling of air pollutants (Shu et al., 2017; Han et al., 2018). The backward trajectory calculation is driven by the one-degree output from NCEP GDAS (<https://ready.arl.noaa.gov/archives.php>). The GDAS data contain 3-hourly basic meteorological fields on pressure surfaces with the spatial resolution of 0.5 degree. 144-h backward trajectories are calculated every six hours (00:00, 06:00, 12:00 and 18:00 UTC). The terminus of these 165 trajectories is set as CCM site in Nanjing at a height of 10 m and 1500 m above the sea level. The levels of 10 m and 1500 m are selected to represent the trajectory arriving altitude near the surface and at the lower troposphere, respectively.

2.4 CAMx model and source apportionment technology

170 **2.4.1 Model description**

Particulate and ozone source apportionment technology (PSAT/OSAT) incorporated in CAMx (version 6.40) are employed to track the source-receptor relationship of PM_{2.5}/O₃ between separate source regions and YRD receptors. CAMx is a three-dimensional Euler grid photochemical model based on UAM-V model, which is developed by the environmental technology company 175 (ENVIRON) (www.camx.com). In addition to typical features shared with other third generation of comprehensive air quality models, CAMx also contains multiple notable extension modules. Source apportionment technology is one of the most famous probing tools in CAMx, which uses the tagging method. PSAT/OSAT has the capability of calculating the hourly contributions of given source regions and categories to the concentrations of PM_{2.5}/O₃ and related precursors at a 180 specified receptor (Yarwood et al., 1996, 2004; Wagstrom, et al., 2008). PSAT uses six tracer families to track the fate of primary and secondary PM, including sulfate, nitrate, ammonium, primary PM, secondary organic aerosol and particulate mercury (the latter two are not considered in this study). OSAT reports information to determine whether each O₃ component formed in NO_x or VOC sensitive conditions. To date, CAMx and PSAT/OSAT have been extensively applied in 185 the simulation and source attribution of regional air pollution within a variety of spatiotemporal scales (Koo et al., 2009; Nopmongcol et al., 2012; Dunker, et al., 2017; Li et al., 2012, 2015b, 2016; Wu et al., 2013a; Wang et al., 2017).

2.4.2 Model setup

The simulation is conducted from 17th August to 14th September and 1st to 22nd December in 190 2016, in which the initial 48 h is taken for spin-up. Two one-way nested domains are designed adopting a Lambert Conformal map projection, with the grid spacing of 27 and 9 km. The outer domain covers most areas of eastern China, while the nested domain covers YRD. For both domains, there are 23 vertical sigma layers from the surface to the top of 100 hPa. Off-line meteorological fields from Weather Research and Forecasting (WRF, version 3.7) are supplied to 195 drive CAMx. WRF is a new generation of meso-scale weather forecast model and assimilation system, developed by the National Center for Atmospheric Research (NCAR). The initial and

boundary meteorological conditions are driven by NCEP/FNL reanalysis data. The configuration options in WRF and emission inventory are consistent with our previous work (Shu et al., 2016). Monthly-based anthropogenic emission inputs of major pollution species (NO_x , SO_2 , primary PM_{2.5}, PM₁₀, black carbon, OC and VOCs) are prepared and obtained from Multi-resolution Emission Inventory for China (MEIC v1.2, <http://www.meicmodel.org>) developed by the Tsinghua University with $0.25^\circ \times 0.25^\circ$ horizontal resolution and five categories (agriculture, industry, power, residential and transportation). Biogenic emissions are calculated by the nature emission model developed by Xie et al. (2007, 2017). The domain setting and configuration options in CAMx are summarized in Table 1. The model performance evaluation is provided in the supplementary.

In PSAT/OSAT, eastern China is subdivided into fifteen source regions, namely 13 provinces (including Shanghai municipality), the BTH region and other areas (Fig. 1). In addition, the initial conditions and boundary conditions (ICBC) are tracked as separated source groupings. Such division of source regions helps to determine local and remotely derived contributions of source groups to pollutants in YRD. The arrows in Fig. 1 clearly demonstrate the different spatial scales of transport of air pollutants. Local transport (local source) generally represents the transport within one province (Jiangsu, Zhejiang, Anhui provinces and Shanghai). The intra- and inter-regional transport represent the transport from regions within YRD (excluding local contribution), and out of YRD within the study domain, respectively. Additionally, the impacts of ICBC could be regarded as the contributions of super-regional transport, including the contributions from upwind precursors emissions transported to YRD which produce PM_{2.5} and O₃, as well as PM_{2.5} and O₃ formed in the transportation process (Li et al., 2012, 2016).

3. Characteristics of PM_{2.5} and O₃

220 3.1 Characterization of PM_{2.5} and O₃ episodes

Figures. 2&3 display the day-to-day variation of PM_{2.5} and daily maximum 8-hour average (MDA8) O₃ in YRD during the CAPUM-YRD, respectively. To better explore the main causes of

PM_{2.5} and O₃ pollution (characteristics and source attribution), two severe PM_{2.5}-polluted episodes and one clean episode are identified according to PM_{2.5} levels in winter, which are termed
 225 PM25_Ep1 (4th-9th December), PM25_Ep2 (16th-20th December) and PM25_Clean (10th-14th December). Similarly, three high O₃ episodes and one clean episode are selected on the basis of summertime O₃ levels, termed O3_Ep1 (24th-25th August), O3_Ep2 (1st-5th September), O3_Ep3 (8th-13th September) and O3_Clean (20th-22nd August). Figure 4 exhibits the average 850 hPa geopotential height field and wind field during different PM_{2.5} and O₃ episodes, while Figure 5
 230 presents the average height-latitude cross-sections of vertical velocity. Figures 6&7 show the hourly variation of main air pollutants and meteorological parameters in Hangzhou during the winter and summer experiment, respectively. Similar graphs for Shanghai, Nanjing and Hefei are provided separately in the supplementary (Figures S1-S6).

3.1.1 PM_{2.5} episodes

235 In winter, PM_{2.5} pollution is dominant in the atmosphere over YRD (Li et al., 2011; Ding et al., 2013; Ming et al., 2017). Daily average PM_{2.5} can easily exceed the NAAQS (75 µg/m³) at more than half of the sites, with frequent occurrence of severe synchronous pollution episodes (over 120 µg/m³) (Fig. 2). In PM25_Ep1, YRD is located at the rear of the East Asian trough and in the front
 240 of an anticyclonic system (Fig. 4a). Strong northwesterly flows can directly transport pollutants from northern China to YRD (Shu et al., 2017), while dominant strong downward motion (26-32°N, see Fig. 5a) inhibits the diffusion of pollution. This episode features the highest PM_{2.5} (99.6 µg/m³ averaged over all sites) and PM₁₀ (158.1 µg/m³) (Table S2), as well as the maximum fire counts detected in YRD (box D02 in Fig. 1). Especially, the highest daily average PM_{2.5} reaches up to 142.3 µg/m³ on 5th December, followed by 141.5 µg/m³ on 8th December at Hefei
 245 LYQ site. During this episode, the transport process of air pollution exhibits the distinctive feature of gradual movement from north to south. In the first part (5th December), Hefei and Nanjing sites are first severely affected when the peak values of PM_{2.5} occurring at 19:00 LT (312.6 and 255.7 µg/m³, respectively, see Figs. S3 and S5), followed by Shanghai (132.5 µg/m³ at 22:00 LT, see Fig.
 S1) and Hangzhou (248.0 µg/m³ at 00:00 LT on 6th December, see Fig. 6). An explosive growth

250 of PM_{2.5} levels occurs, especially in Hefei, Nanjing and Hangzhou. The prevailing northerly winds and rapid increase in wind speed and PM components (OC, EC in Nanjing) suggest the significant transport of pollutants from the north. Besides, the extremely high levels of NO₂ ahead of the peak of PM_{2.5} in Hangzhou indicate that secondary transformation could play a vital role in the explosive growth of PM_{2.5} (Fig. 6). In the second part (7th-9th December), there appears an
255 accumulated growth in PM_{2.5} concentrations attributed to stagnant conditions (high RH, comparatively weak wind) and possibly haze moving across YRD from the west towards the east (northwesterly wind during the nighttime, see Figs. 6, S1 and S3). Further, the pollution process pattern of PM25_Ep2 is reversed, when YRD is affected by a strong anticyclonic system centered above the East China Sea (Fig. 4b) and weaker downward motion (Fig. 5b). The ground south
260 wind (16th-18th December) gradually shifts to the northeast-north wind (19th-20th December) (Figs. 6, S1, S3 and S5). Correspondingly, the highest levels of PM_{2.5} are observed in coastal cities right at the outset (south wind) and then peak values are found in Hefei in the second part (northeast-north wind). Higher RH is observed in PM25_Ep2 compared to PM25_Ep1, especially during the nighttime (Table S3). Worthy of note, PM_{2.5} pollution gets worse at midnight on 19th
265 December before the rainfall during 20th-21st December accompanied with the invasion of cold air from the north (Figs. 6, S1 and S3). The abundant accumulated precursors and moisture favor the hygroscopic growth of particles. Generally, regional average PM_{2.5} and PM₁₀ concentrations are respectively 94.0 and 135.5 $\mu\text{g}/\text{m}^3$, along with fewer fire counts detected in YRD contrasting with PM25_Ep1 (Fig. 2). In PM25_Clean, the southeast China is controlled by a notably weak
270 high-pressure system (Fig. 4c), while weaker downdrafts (30-32°N) and stronger updrafts (32-32.5°N) dominate above YRD (Fig. 5c). The anticyclonic circulation leads to the prevailing northeast-north wind (Figs. 6, S1, S3 and S5), weak radiation (Fig. 6), cloudy weather (Fig. S5) and regional rainfalls (on 13th December, see Figs. 6, S1 and S3) over YRD. The slightly enhanced PM_{2.5} pollution during the nighttime (12th-13th December) is easily relieved by the
275 rainfall (wet removal processes) and strong northerly wind (dry removal processes) during 13th-15th December. As for O₃, wintertime O₃ levels theoretically maintain low values due to low temperature and weak photochemical reaction (Fig. 3). However, relatively high O₃ (especially

Shanxilu (SXL) site) and remarkable spatial heterogeneity are observed in Nanjing. SXL site is located in the bustling downtown and suffers from heavy traffic emission due to dense bus routes.

280 The significant heterogeneity of O₃ levels in a single city implies the importance of local emission at a finer scale (such as street scale).

3.1.2 O₃ episodes

In summer, O₃ pollution becomes extremely prominent ascribed to the favorable weather conditions (high temperature, strong radiation, etc). In O3_Ep1, a strong cyclone (Typhoon 285 Lionrock, forms on 18th August and dissipates on 30th August) is detected over the western Pacific Ocean (http://weather.unisys.com/hurricane/w_pacific/2016/index.php), the development and movement of which profoundly influence weather conditions and air pollution along southeastern China. Due to cyclonic circulation (Fig. 4d), surface easterly wind prevails over YRD (Figs. 7, S2, S4 and S6). Stagnant conditions (higher T, low humidity and weaker surface wind) 290 occur at specific sites controlled by downward flows (Fig. 5d) related to the peripheral circulation of the typhoon (Shu et al., 2016), which favors the occurrence of extremely high O₃ in Nanjing and Hefei (Figs. S4 and S6, Table S3). O₃ pollution is the most serious during this episode, with regional average MDA8 O₃ reaching 211.1 μg/m³. Impressively, MDA8 O₃ reaches above 300 μg/m³ at SXL, Ruijinlu (RJL) and CCM sites in Nanjing on 25th August. Afterward, Typhoon 295 Lionrock makes its landfall in northeastern Japan on 30th August and then develops into an extratropical cyclone, which is centered in northeastern China in O3_Ep2 (Fig. 4e). Evident downdrafts above YRD (28-32°E) help to trap the heat as well as air pollutants within the planetary boundary layer (PBL) (Fig. 5e). At the surface, the southwesterly wind (1st-2nd September) gradually shifts to weaker easterly wind (3rd-5th September). During this episode, the 300 persistent high O₃ is observed in Shanghai and Nanjing with regional average MDA8 O₃ reaching 184.0 μg/m³. Additionally, YRD suffers from obviously heavier PM_{2.5} (55.1 μg/m³) and PM₁₀ (109.1 μg/m³) pollution (Table S2), with relatively higher EC and OC observed in Shanghai and Nanjing. However, the detected fire counts show a poor correlation with PM_{2.5} levels in summer (Fig. 2), implying the difference in major source contributors to PM pollution during different

305 seasons. O₃_Ep3 features a high-pressure system at 850 hPa over YRD (Fig. 4f), with enhanced downdrafts (28-32°E, see Fig. 5f) and the highest surface air pressure (Figs. S2 and S4). High RH and comparatively lower temperature are found in Shanghai and Hangzhou (Figs. 7 and S2) related to southerly-easterly winds. Overall, regional average MDA8 O₃ is 171.5 µg/m³ in O₃_Ep3. Substantial spatial heterogeneity of O₃ occurs, where comparably low O₃ is found in Hangzhou 310 and Shanghai on 10th-11th September ascribed to cloudy/rainy weather (Figs. 7 and S2). Meantime, enhanced surface wind (peak at 14:00 LT on 11th September) leads to the sharp decrease in temperature and concentrations of major pollutants in Nanjing (Fig. S4). In contrast, O₃ concentrations maintain high levels in Hefei during 10th-12th September regardless of the 315 strong wind and partial cloud cover (Fig. S6). The spatial heterogeneity of O₃ levels among different cities behaves much more evident in O₃_Clean when northwest wind prevails over YRD owing to the circulation pattern of double low-pressure systems (Fig. 4g). Distinct ascending motion above the latitude of 32-32.5° (Fig. 5g) favors the diffusion of pollutants in northern YRD. Consequently, strong rainfall in Nanjing (>15 mm/h, see Fig. S4) and cloudy weather in Hefei 320 (Fig. S6) result in lighter O₃ pollution. However, despite the heavy rainfall in Hangzhou (>25 mm/h at 17:00 LT on 21st August, see Fig. 7) and weaker rainfall in Shanghai (Fig. S2), the persistent, relatively higher O₃ levels are observed in these two cities, exhibiting a stark contrast to other cities. On the whole, the regional feature of PM pollution is much more distinctive. In comparison, significant spatial heterogeneity exists in O₃ pollution among different sites/cities, 325 owing to the differences in local meteorological conditions (radiation, temperature and wind), as well as local emission and regional transport.

3.1.3 Diurnal patterns

Figure 8 demonstrates the diurnal variations of main air pollutants and meteorological parameters during different episodes. In general, the time dependencies on emission and local meteorological conditions can be important factors controlling the diurnal patterns of pollutants. The diurnal cycle 330 of PM_{2.5} is primarily governed by boundary layer dynamics (Quan et al., 2013; Li et al., 2017b). In winter, the diurnal profiles of PM_{2.5} present distinct differences between polluted and clean

episodes. In polluted days, high PM_{2.5} levels usually persist through the night until the morning, owing to the formation of the nocturnal inversion layer, stable PBL and weakened surface wind (Table S3) during the nighttime. After the noon, PM_{2.5} concentrations gradually decrease and 335 reach the minimum at around 16:00 LT, associated with the deeper PBL depth and favorable diffusion conditions (Wang et al., 2014; Petäjä et al., 2016). PM25_Ep1 features the largest daily range of PM_{2.5}, with dramatically high PM_{2.5} in the evening (19:00 LT) ascribed to the explosive growth of PM_{2.5} on 5th December over YRD (Figs. S3 and S5). Further, the diurnal cycle of O₃ follows the unimodal pattern, controlled by the diurnal pattern of radiation. The maximum O₃ is 340 usually observed during 14:00-15:00 LT due to higher temperature and active photochemical reactions. The minimum of O₃ is observed at around 07:00 LT ascribed to the continuous depletion by NO_x during the nighttime. Worthy of note, PM25_Ep1 also has the largest diurnal change of O₃, related to more favorable weather conditions (higher T, lower RH and weaker wind) and massive depletion of precursor during the daytime (Fig. 8 and Table S3). Moreover, the 345 diurnal variation of NO₂, EC and OC show certain consistency with that of PM_{2.5} in PM25_Ep1, with the dramatic increase from 14:00 to 19:00 LT. The highest SO₂ is usually found in the late morning (10:00-11:00 LT) when PBL mixing height is well developed, since SO₂ is mostly emitted from elevated sources like power plant (Ding et al., 2013). In contrast, the diurnal variations of all pollutants in PM25_Clean are less obvious related to rainy/cloudy weather and 350 stronger surface wind (Figs. 6, S1, S3 and S5).

In summer, the diurnal cycles of PM_{2.5} (except O₃_Ep1) are similar to that in winter, with the minimum at 16:00-17:00 LT. The rapid increase in PM_{2.5} is obvious in O₃_Ep2, in accordance with heavier PM pollution in this episode (Table S2). Besides, the weak peak of PM_{2.5} at 08:00 LT could be attributed to the possible influence of morning traffic emission. Furthermore, the diurnal 355 cycle of summertime O₃ is more pronounced, especially the evident broad peak of daytime O₃ (11:00-18:00 LT) due to the long duration of high temperature and strong radiation (Figure S7). In particular, high T, relatively low RH and the strongest radiation (Table S3) favor the occurrence of the most serious O₃ pollution in O₃_Ep1 (Pu et al., 2017). The minimum of O₃ level during the morning hours occurs at 06:00 LT, linked to the earlier sunrise in summer. As the O₃ precursor,

360 the NO₂ variation is exactly contrary to ozone with a weak morning peak during the rush hours (at 07:00 LT). In addition, NO₂, SO₂, EC and OC levels get increased after sunset in O3_Ep2, corresponding to the elevated PM_{2.5} levels.

3.2 Characteristics of PM_{2.5} components

3.2.1 Secondary inorganic components

365 Secondary inorganic components in PM_{2.5}, especially sulfate, nitrate and ammonium (SNA), play a significant role in ambient air quality (Wang et al., 2005; Ming et al. 2017). The sulfur oxidation ratio (SOR: the ratio of [nSO₄²⁻] to [nSO₄²⁻ + nSO₂], n refers to molar concentration) and nitrogen oxidation ratio (NOR: the ratio of [nNO₃⁻] to [nNO₃⁻ + nNO₂]) are applied to evaluate the degree of secondary conversion from SO₂ to SO₄²⁻, and NO_x to NO₃⁻, respectively (Hua et al., 2015).

370 Figure 9 illustrates the comparison of SOR, NOR, SO₄²⁻ and NO₃⁻ during different episodes. Generally, SNA accounts for a substantial proportion of 49.3% and 55.3% in PM_{2.5} during the summer and winter experiments, respectively. In winter, the concentrations of NO₃⁻ are strikingly higher than SO₄²⁻ during high PM_{2.5} episodes. The average NO₃⁻ and SO₄²⁻ concentrations are 21.7 and 13.6 $\mu\text{g}/\text{m}^3$ in PM25_Ep1, 22.0 and 11.5 $\mu\text{g}/\text{m}^3$ in PM25_Ep2, respectively. The average NOR 375 and SOR are respectively 0.16 and 0.24 in winter, with a clear increase in polluted days. PM25_Ep1 has the highest NOR (0.18) and SOR (0.28), followed by PM25_Ep2 (0.17 and 0.26, respectively). In comparison, PM25_Ep1 features moderate ambient humidity (Fig. 9 and Table S3), which enhances the absorption of gaseous precursors (especially hydrophilic SO₂ and NO₂) and avoids wet deposition caused by excessive humidity. Besides, the sharp increase of particles per unit volume provides a sufficiently large interface, which favors the formation of SNA 380 through heterogeneous aqueous uptake of precursors (Wang et al., 2012). The integrated effect of above favorable conditions leads to the explosive growth of PM_{2.5} in PM25_Ep1. In summer, NO₃⁻ concentrations are generally lower than SO₄²⁻ contrasting with winter (Fig. 9), which might be explained by the volatility and evaporative loss of nitrate (Sun et al., 2012). SO₄²⁻ concentration is 385 the highest in O3_Ep2 (13.0 $\mu\text{g}/\text{m}^3$), while NO₃⁻ and NH₄⁺ levels reach the maximum in O3_Ep3

(11.9 and 8.4 $\mu\text{g}/\text{m}^3$, respectively). A weakened conversion from NO_2 to nitrate (0.09) is observed, with the maximum in O3_Ep3 (0.15) and minimum in O3_Ep1 (0.07). In contrast, an enhanced conversion from SO_2 to sulfate (0.31) occurs, especially in O3_Ep2 (0.39) and O3_Ep3 (0.39). Worthy of note, stagnant conditions (weak radiation and T, weak wind, see Table S3) and high RH are conducive to the heterogeneous formation and local accumulation of SNA, leading to high NOR and SOR in O3_Ep3.

Furthermore, to exclude the impacts from significant regional transport of sulfate and nitrate (Ying et al., 2014), the ‘local’ SOR and NOR are calculated on the basis of simulated concentrations contributed by local emissions (refer to PSAT results) as listed in Table 2. 395 Generally, the newly defined SOR and NOR are distinctively lower (< 0.1) than traditional results calculated using observation data, which implies the significant regional transport of secondary inorganic components of $\text{PM}_{2.5}$ and gaseous precursors. Local SOR values vary within the range of 0.067-0.071 (0.067-0.086) among winter (summer) episodes. In contrast, local NOR is generally higher in winter (0.040-0.066) than summer (0.036-0.051), consistent with observational 400 results.

3.2.2 Carbonaceous components

Table 3 lists carbonaceous fraction (OC and EC) in $\text{PM}_{2.5}$ and the OC to EC ratio (OC/EC) in Shanghai and Nanjing sites, compared with recent studies (published during 2015-2017) in YRD cities. In general, total carbonaceous components (OC+EC) account for 16.8% (21.3%) of $\text{PM}_{2.5}$ 405 in Shanghai, and 27.8% (21.5%) in Nanjing during the summer (winter) experiment. In Shanghai, OC and EC concentrations at DSL site are slightly higher (lower) than PD site in summer (winter). However, the OC/EC values are comparable at these two sites, higher in summer (5.0~5.1) than winter (2.9~3.1). Compared to previous studies in Shanghai, Wang et al. (2016) also found the highest OC/EC (3.2) during summer of 2012, while Ming et al. (2017) reported remarkably higher 410 OC/EC of $\text{PM}_{2.5}$ in summer (6.0) and winter (6.9) during 2013-2014. In Nanjing, OC and EC concentrations are higher at CCM site in winter than summer (Table 3). The seasonal pattern of OC/EC in Nanjing is consistent with Shanghai, where higher OC/EC in summer (2.1) and lower

values in winter (1.7) are observed. The results are comparable with those reported by Chen et al. (2017) that OC/EC values ranging from 1.6~2.8 are observed in Nanjing during 2013-2015. The lower OC/EC ratio in Nanjing compared to Shanghai is potentially ascribed to larger VOCs emission in Shanghai. Fu et al. (2013) revealed that anthropogenic VOC emission in Shanghai during 2010 is nearly 2.5 times that in Nanjing, resulting in the addition of SOA to OC. Further, secondary organic carbon (SOC) concentrations are estimated based on the EC-tracer method (Castro et al., 1999), while the ratio of SOC to OC (SOC/OC) is calculated as well (Table S4). The order of average SOC/OC is PD (66.3%/63.6%) > DSL (49.4%/60.8%) > CCM (40.4%/57.0%) in winter/summer. The high OC/EC and SOC/OC in Shanghai suggest the importance of secondary transformation in PM_{2.5} pollution, especially in the suburban site. Worthy of note, the highest OC/EC (5.2~5.8) and SOC/OC (61.5~69.7%) are found in O3_Ep1, where the lowest slopes of $\Delta\text{OC}/\Delta\text{EC}$ (0.36) and poor correlation are found as well (Figure S8). The enhanced SOC formation should be responsible for the poor correlation and it implies more complicated and varied sources.

4. Source attribution of PM_{2.5} and O₃

4.1 Backward trajectory analysis

Figure 10 displays the 144-h backward trajectories ending at 10 m and 1500 m, along with fire counts during different episodes. It can provide a visual insight into the source of air masses arriving YRD. In winter, PM25_Ep1 is dominated by northwesterly sources through long-range transport, when trajectories arriving at the lower troposphere seldom have land contact (Fig. 10a) owing to strong downward motion (Fig. 5a). Continental trajectories (northern and central China) associated with the invasion of cold, dry air brought by the strong Siberia High may enhance the air pollution over YRD, when intensive fire counts are detected along pathways and in YRD (Fig. 10a). PM25_Ep2 corresponds to northwesterly origins, more land contacts with marine areas and neighboring provinces, and fewer fire counts. The frequent contacts of flows arriving at the lower troposphere (Fig. 10b) with the surface suggest weaker downward motion compared to PM25-

440 _Ep1. PM_{2.5}_Clean has the most northeasterly marine trajectories and obvious upward motion (Figs. 10c and 5c). More marine sources and favorable vertical diffusion condition contribute to the surface rainfall (Figs. 6, S1 and S3) and the mitigation of pollution over YRD.

In summer, O₃_Ep1 is dominated by surface easterly winds (Figs. 7, S2, S4 and S6) and northerly trajectories originated from northeastern China traveling over vast oceanic areas (Fig. 445 10d). Marine flows could effectively mitigate PM_{2.5} pollution over YRD. However, the high O₃ levels (especially in Nanjing and Hefei, see Figs. S4 and S6) suggest the possible contribution by long-regional transport of pollutants. O₃_Ep2 and O₃_Ep3 feature more northwesterly origins at the lower troposphere (Figs. 10e-f). In contrast, most trajectories arriving surface are found within PBL (< 2 km) in O₃_Ep2 (Fig. 10e), while prominent downward flows occur in O₃_Ep3 (Fig. 450 10f). It suggests the different relative importance of source regions to severe O₃ pollution during these two episodes. O₃_Clean shares certain similarities in transport compared with O₃_Ep1. However, more contact time of trajectories over the ocean occurs, while the transport generally takes place within PBL (<1 km) in O₃_Clean (Fig. 10g). Consequently, abundant marine air masses and significant convective activity (Fig. 10g) result in cloudy/rainy weather (Figs. 7, S2 455 and S6) and weak O₃ production (Figs. 4 and S6) over YRD.

4.2 Source apportionment

4.2.1 Source region contributions to PM_{2.5} and its components

Further, PSAT/OSAT is applied to identify the quantitative contributions of different source regions to PM_{2.5}/O₃ concentrations over YRD. Figure 11 displays the average source region 460 contributions to PM_{2.5}, inorganic components of PM_{2.5} and daytime O₃ of DSL, ZH, CCM and LYQ sites during different episodes of the CAPUM-YRD. Generally, local contribution (within a province) accounts for a significant proportion in PM_{2.5} and its components. Particularly, local emissions from Zhejiang (Anhui) province overwhelmingly contributes over 50% to PM_{2.5} 465 concentrations of ZH (LYQ) sites during all episodes. Moreover, the relative importance of regional transport to PM_{2.5} shows distinctive variability during different episodes. In winter, the intra- and inter- regional transport of air pollutants are most notable in PM_{2.5}_Ep1. For example,

PM_{2.5} concentrations at DSL site are greatly contributed by emissions from Jiangsu (31.8%), Zhejiang (20.4%) and Anhui (10.8%) provinces. Meantime, the transport of pollutants from Anhui province has large impacts on PM_{2.5} concentrations of CCM site (34.0%). Further, the 470 inter-regional transport of pollutants, especially from the north-northwest (BTH, Shandong, Henan and Hubei provinces), can generally contribute over 20% in PM_{2.5} over YRD, which is in the order of CCM (28.4%) > DSL (25.7%) > ZH (24.4%) > LYQ (24.3%). In PM25_Ep2, PM_{2.5} pollution over YRD is influenced by more local emissions owing to weaker surface wind (Table S3). The intra-regional contributions from Jiangsu province to PM_{2.5} concentrations of ZH (11.5%) and 475 LYQ (13.3%) sites also get intensified due to the strong anticyclonic circulation (Fig. 4b). Besides, the long-range transport from the north (Shandong province and BTH) is more prominent with fewer pollutants transported from the northwest to YRD contrasting with PM25_Ep1. In PM25_Clean, PM_{2.5} concentrations in YRD are mostly contributed by emissions locally and intra-regionally. Worthy of note, due to the transport from northeastern China (Figs. 10c-d), 480 emissions from Liaoning province exert weak impacts on PM_{2.5} concentrations (1.5-2.9%) in YRD, while similar results are found in O₃_Ep1 (1.1-1.8%). In summer, the relative importance of source regions shows certain similarities compared to PSAT results in winter. The local and intra-regional contributions dominate in PM_{2.5} concentrations (70-90%) in O₃_Ep2 and O₃_Ep3. The impacts of inter-regional transport from outside regions (Shandong, Hubei and Henan 485 provinces) are prominent as well (17.6-19.4% and 5.6-9.6% respectively for O₃_Ep2 and O₃_Ep3). In contrast, local contribution accounts for a larger proportion in PM_{2.5}, reaching above 90% at CCM site (94.5%) in O₃_Ep1 and ZH site (94.2%) in O₃_Clean.

With respect to inorganic components of PM_{2.5}, the relative importance of source regions to SO₄²⁻ show great similarities to PM_{2.5} in winter. In summer, the intra-regional contributions 490 (Hubei, Henan and Shandong provinces) make up a significant proportion in SO₄²⁻ in O₃_Ep2 (32.9-37.6%) and O₃_Ep3 (15.1-22.4%). In contrast, higher contributions of emissions from outside regions (BTH, Shandong, Henan and Hubei provinces) to wintertime NO₃⁻ in YRD are found, especially in PM25_Ep1 (33.9-39.1%). Moreover, NO₃⁻ concentrations are more likely to be contributed by super-regional transport (1.2-5.7%) compared to PM_{2.5} and other inorganic

495 components. In comparison, the formation of NH_4^+ is remarkably associated with local emissions
 (agriculture sources) in YRD.

4.2.2 Source region contributions to O_3

Compared OSAT with PSAT results, the super-regional transport plays a more significant role in
 O_3 over YRD as illustrated in Fig. 11, with the average contribution of 29.4-50.7% (31.8-39.0%)
 500 during PM_{2.5} (O_3) episodes. High values of super-regional contributions are found in PM25_Clean
 and O₃_Ep1 under the great impacts of northeasterly flows (Figs. 10c-d), especially at coastal
 DSL site (48.4% and 63.0%, respectively). In O₃_Ep1, the relative contributions of local and
 intra- transport vary from 42.7% (DSL) to 63.4% (LYQ), while emissions from Liaoning province
 (related to northeasterly trajectories, see Fig. 10d) accounts for a small proportion in O₃
 505 concentrations (2.8-4.7%) in accordance with PSAT results. The extremely high O₃ levels during
 this episode may be largely due to the intra- and super-regional transport. In O₃_Ep2 and O₃_Ep3,
 local and regional transport of pollutants are jointly responsible for high O₃ in YRD. It is
 noteworthy that the inter-regional contributions of emission from the north-northwest (BTH,
 Shandong, Henan and Hubei provinces) are within the range of 17.3-21.4% and 10.8-14.2% in
 510 O₃_Ep2 and O₃_Ep3, respectively. The larger contribution in O₃_Ep2 is exactly due to the
 significant transport near the surface within PBL (Fig. 10e). In O₃_Clean, local contributions
 (30.2-59.4%) dominate in O₃ concentrations over YRD, followed by super-regional contribution
 (27.4-38.4%). In winter, the relative contributions of local and intra-regional transport in YRD are
 515 in the range of 55.1-58.3%, 43.6-67.1% and 29.9-48.1% in PM25_Ep1, PM25_Ep2 and
 PM25_Clean, respectively. The inter-regional transport from the northwest-north contributes most
 to O₃ concentrations (10.9-14.4%) in PM25_Ep1, with a maximum at CCM site.

5. Summary

This paper focuses on regional PM_{2.5} and O₃ pollution episodes in YRD of eastern China during
 520 two intensive field experiments during the CAPUM-YRD, covering a summer photochemical
 pollution period (14th August to 15th September) and a winter haze pollution period (24th

November to 23rd December) in 2016. Regional PM_{2.5} and O₃ pollution episodes are characterized based on observations at 22 super/national monitoring sites, as well as synoptic analysis of atmospheric circulation and meteorological conditions. Further, trajectory simulation and
 525 PSAT/OSAT in CAMx are applied to qualitatively and quantitatively explore the potential impacts of emissions from different source regions on air pollution over YRD through transport. Generally, the transport of pollutants is differentiated as several spatial scales, including local (within a province), intra-regional (out of a province within YRD), inter-regional (out of YRD within eastern China) and super-regional (out of eastern China) transport. Overall, the major
 530 findings are concluded as follows.

1. PM_{2.5} pollution dominates over YRD in winter, featured by regional synchronous severe episodes (over 120 $\mu\text{g}/\text{m}^3$). Explosive growth in PM_{2.5} occurs under enhanced northerly winds throughout YRD, showing clear evidence for the impact of transport from northern China. The most polluted episode processes the distinctive feature of gradual movement from north to south,
 535 where the peak values of PM_{2.5} are firstly observed in Hefei and in Nanjing. The MODIS fire counts detected over YRD show good (poor) correlation with PM_{2.5} levels in winter (summer).

2. Secondary inorganic and carbonaceous components constitute a major fraction in PM_{2.5} masses (70-80%). The secondary conversion of sulfur (SOR) and nitrogen (NOR) are 0.31 and 0.09 in summer, 0.24 and 0.16 in winter, respectively. Stronger secondary transformation of
 540 gaseous precursors occurs alongside elevated PM_{2.5} levels, where the heterogeneous aqueous reactions may play a crucial role. High OC/EC ratios (5.0~5.1) and SOC/OC (60.8~63.6%) are found in Shanghai in summer, especially at a suburban site (Pudong).

3. Notable regional O₃ pollution exhibits a broad peak during the daytime (11:00-18:00 LT) in summer. Significant spatial heterogeneity of O₃ exists among different sites/cities in YRD.
 545 High O₃ levels are usually found in Nanjing, with MAD8 O₃ reaching over 300 $\mu\text{g}/\text{m}^3$. Stagnant weather conditions (evident downward motions, high T, strong radiation and weak surface wind) favors the occurrence of high O₃ episodes.

4. PSAT results suggest the dominance of local and intra-regional contributions (over 60%) to PM_{2.5} over YRD, while summertime PM_{2.5} is greatly affected by local emissions (over 90%).

550 Moreover, under the control of north-northwest flows and strong downdrafts, the inter-regional transport of pollutants can significantly reinforce PM_{2.5} pollution over YRD. Contributions of outside source regions (including BTH, Shandong, Henan and Hubei provinces) can make up over 20% in PM_{2.5}, with a maximum of 28.4% in Nanjing.

555 5. OSAT results emphasize the significant impact of super-regional transport on daytime O₃ over YRD, varying from 29.4% to 50.7% during different episodes. Particularly, the larger contribution of super-regional transport is usually found in Shanghai (30.3-63.0%) compared to other cities.

560 This study provides an in-depth understanding of regional PM_{2.5} and O₃ pollution episodes in YRD, one of the most developed city clusters in China. The significant synthetic effects of local/regional transport at diverse spatial scales on PM_{2.5} and O₃ pollution in YRD are emphasized. It reveals great challenges in the prevention and control of regional PM_{2.5} and O₃ pollution, especially for O₃, owing to the considerable super-regional contribution. Therefore, enhanced regional collaboration and efforts are fundamental in formulating pollution control strategies.

565 Acknowledgments

This work was supported by the National Natural Science Foundation of China (91544230, 41575145 and 41621005) and the National Key Research and Development Program of China (2016YFC0203303, 2016YFC0208504, 2017FYC0209803 and 2017YFC0210106). The authors would like to thank Shanghai Environmental Monitoring Center, Nanjing Environmental 570 Monitoring Center, Hangzhou Environmental Monitoring Center and Hefei Environmental Monitoring Center for providing observation data, and the anonymous reviewers for their constructive and precious comments on this manuscript.

575 **References**

- Cai, S., Wang, Y., Zhao, B., Wang, S., Chang, X., and Hao, J., 2017. The impact of the “Air Pollution Prevention and Control Action Plan” on PM_{2.5} concentrations in Jing-Jin-Ji region during 2012–2020. *Sci. Total Environ.* 580, 197-209. <https://doi.org/10.1016/j.scitotenv.2016.11.188>.
- Castro, L.M., Pio, C.A., Harrison, R.M., Smith, D.J.T., 1999. Carbonaceous aerosol in urban and rural European atmospheres: estimation of secondary organic carbon concentrations. *Atmos. Environ.* 33, 2771-2781. [https://doi.org/10.1016/S1352-2310\(98\)00331-8](https://doi.org/10.1016/S1352-2310(98)00331-8).
- Chan, C. K., and Yao, X., 2008: Air pollution in mega cities in China. *Atmos. Environ.* 42, 1-42. <https://doi.org/10.1016/j.atmosenv.2007.09.003>.
- Chen, D., Cui, H., Zhao, Y., Yin, L., Lu, Y., and Wang, Q., 2017. A two-year study of carbonaceous aerosols in ambient PM_{2.5} at a regional background site for western Yangtze River Delta, China. *Atmos. Res.* 183, 351-361. <https://doi.org/10.1016/j.atmosres.2016.09.004>.
- Ding, A. J., Fu, C. B., Yang, X. Q., Sun, J. N., Zheng, L. F., Xie, Y. N., Herrmann, E., Nie, W., Petäjä, T., Kerminen, V. M., and Kulmala, M., 2013. Ozone and fine particle in the western Yangtze River Delta: an overview of 1 yr data at the SORPES station. *Atmos. Chem. Phys.* 13, 5813-5830. <https://doi.org/10.5194/acp-13-5813-2013>.
- Draxler, R., and Rolph, G., 2013. HYSPLIT (HYbrid Single-Particle Lagrangian Integrated Trajectory), NOAA Air Resources Laboratory, College Park, MD, Model access via NOAA ARL READY Website.
- Dunker, A. M., Koo, B., and Yarwood, G., 2017. Contributions of foreign, domestic and natural emissions to US ozone estimated using the path-integral method in CAMx nested within GEOS-Chem. *Atmos. Chem. Phys.* 17, 12553-12571. <https://doi.org/10.5194/acp-17-12553-2017>.
- Feng, L., and Liao, W., 2016. Legislation, plans, and policies for prevention and control of air pollution in China: achievements, challenges, and improvements. *J. Clean. Prod.* 112, 1549-1558. <https://doi.org/10.1016/j.jclepro.2015.08.013>.
- Fornacca, D., Ren, G., and Xiao, W., 2017. Performance of Three MODIS Fire Products (MCD45A1, MCD64A1, MCD14ML), and ESA Fire_CCI in a Mountainous Area of Northwest Yunnan, China, Characterized by Frequent Small Fires. *Remote Sens.* 9, 1131. <https://doi.org/10.3390/rs9111131>.
- Fu, X., Cheng, Z., Wang, S., Hua, Y., Xing, J., and Hao, J., 2016. Local and regional contributions to fine particle pollution in winter of the Yangtze River Delta, China. *Aerosol Air Qual. Res.* 16, 1067-1080. <https://doi.org/10.4209/aaqr.2015.08.0496>.
- Fu, X., Wang, S., Zhao, B., Xing, J., Cheng, Z., Liu, H., and Hao, J., 2013. Emission inventory of primary pollutants and chemical speciation in 2010 for the Yangtze River Delta region, China. *Atmos. Environ.* 70, 39-50. <https://doi.org/10.1016/j.atmosenv.2012.12.034>.
- Gao, J., Zhu, B., Xiao, H., Kang, H., Hou, X., and Shao, P., 2016. A case study of surface ozone source apportionment during a high concentration episode, under frequent shifting wind conditions over the Yangtze River Delta, China. *Sci. Total Environ.* 544, 853-863. <https://doi.org/10.1016/j.scitotenv.2015.12.039>.
- Giglio, L., Schroeder, W., and Justice, C. O., 2016. The collection 6 MODIS active fire detection algorithm and fire products. *Remote Sens. Environ.* 178, 31-41. <https://doi.org/10.1016/j.rse.2016.02.054>.
- Han, H., Liu, J., Yuan, H., Zhuang, B., Zhu, Y., Wu, Y., Yan, Y., and Ding, A., 2018b. Characteristics of intercontinental transport of tropospheric ozone from Africa to Asia. *Atmos. Chem. Phys.* 18, 4251-4276,

- 615 https://doi.org/10.5194/acp-18-4251-2018.
- Hu, J., Wang, Y., Ying, Q., and Zhang, H., 2014. Spatial and temporal variability of PM_{2.5} and PM₁₀ over the North China Plain and the Yangtze River Delta, China. *Atmos. Environ.* 95, 598-609. <https://doi.org/10.1016/j.atmosenv.2014.07.019>.
- 620 Hua, Y., Cheng, Z., Wang, S., Jiang, J., Chen, D., Cai, S., Fu, X., Fu, Q., Chen, C., Xu, B., and Yu, J., 2015. Characteristics and source apportionment of PM_{2.5} during a fall heavy haze episode in the Yangtze River Delta of China. *Atmos. Environ.* 123, 380-391. <https://doi.org/10.1016/j.atmosenv.2015.03.046>.
- Jiang, F., Zhou, P., Liu, Q., Wang, T., Zhuang, B., and Wang, X., 2012. Modeling tropospheric ozone formation over East China in springtime. *J. Atmos. Chem.* 69, 303-319. <https://doi.org/10.1007/s10874-012-9244-3>.
- Kan, H., Chen, R., and Tong, S., 2012. Ambient air pollution, climate change, and population health in China. *Environ. Int.* 42, 10-19. <https://doi.org/10.1016/j.envint.2011.03.003>.
- 625 Koo, B., Wilson, G. M., Morris, R. E., Dunker, A. M., and Yarwood, G., 2009. Comparison of Source Apportionment and Sensitivity Analysis in a Particulate Matter Air Quality Model. *Environ. Sci. Technol.* 43, 6669-6675. <https://doi.org/10.1021/es9008129>.
- Li, B., Zhang, J., Zhao, Y., Yuan, S., Zhao, Q., Shen, G., and Wu, H., 2015a. Seasonal variation of urban carbonaceous aerosols in a typical city Nanjing in Yangtze River Delta, China. *Atmos. Environ.* 106, 223-231. <https://doi.org/10.1016/j.atmosenv.2015.01.064>.
- 630 Li, L., Chen, C. H., Fu, J. S., Huang, C., Streets, D. G., Huang, H. Y., Zhang, G. F., Wang, Y. J., Jang, C. J., Wang, H. L., Chen, Y. R., and Fu, J. M., 2011. Air quality and emissions in the Yangtze River Delta, China. *Atmos. Chem. Phys.* 11, 1621-1639. <https://doi.org/10.5194/acp-11-1621-2011>.
- 635 Li, L., An, J. Y., Zhou, M., Yan, R. S., Huang, C., Lu, Q., Lin, L., Wang, Y. J., Tao, S. K., Qiao, L. P., Zhu, S. H., and Chen, C. H., 2015b. Source apportionment of fine particles and its chemical components over the Yangtze River Delta, China during a heavy haze pollution episode. *Atmos. Environ.* 123, 415-429. <https://doi.org/10.1016/j.atmosenv.2015.06.051>.
- 640 Li, L., An, J. Y., Shi, Y. Y., Zhou, M., Yan, R. S., Huang, C., Wang, H. L., Lou, S. R., Wang, Q., Lu, Q., and Wu, J., 2016. Source apportionment of surface ozone in the Yangtze River Delta, China in the summer of 2013. *Atmos. Environ.* 144, 194-207. <https://doi.org/10.1016/j.atmosenv.2016.08.076>.
- 645 Li, M., Hu, M., Du, B., Guo, Q., Tan, T., Zheng, J., Huang, X., He, L., Wu, Z., and Guo, S., 2017a. Temporal and spatial distribution of PM_{2.5} chemical composition in a coastal city of Southeast China. *Sci. Total Environ.* 605-606, 337-346. <https://doi.org/10.1016/j.scitotenv.2017.03.260>.
- Li, Y., Lau, A. K. H., Fung, J. C. H., Zheng, J. Y., Zhong, L. J., and Louie, P. K. K., 2012. Ozone source apportionment (OSAT) to differentiate local regional and super-regional source contributions in the Pearl River Delta region, China. *J. Geophys. Res.* 117, D15305. <https://doi.org/10.1029/2011JD017340>.
- 650 Li, Z., Guo, J., Ding, A., Liao, H., Liu, J., Sun, Y., Wang, T., Xue, H., Zhang, H., and Zhu, B., 2017b. Aerosol and boundary-layer interactions and impact on air quality. *Natl. Sci. Rev.* 4, 810-833. <https://doi.org/10.1093/nsr/nwx117>.
- Liang, L., Engling, G., Zhang, X., Sun, J., Zhang, Y., Xu, W., Liu, C., Zhang, G., Liu, X., and Ma, Q., 2017. Chemical characteristics of PM_{2.5} during summer at a background site of the Yangtze River Delta in China. *Atmos. Res.* 198, 163-172. <https://doi.org/10.1016/j.atmosres.2017.08.012>.
- 655 Liu, X.-H., Zhang, Y., Cheng, S.-H., Xing, J., Zhang, Q., Streets, D. G., Jang, C., Wang, W.-X., and Hao, J.-M., 2010a. Understanding of regional air pollution over China using CMAQ, part I performance evaluation and seasonal variation. *Atmos. Environ.* 44, 2415-2426. <https://doi.org/10.1016/j.atmosenv.2010.03.035>.

- Liu, X.-H., Zhang, Y., Xing, J., Zhang, Q., Wang, K., Streets, D. G., Jang, C., Wang, W.-X., and Hao, J.-M., 2010b. Understanding of regional air pollution over China using CMAQ, part II. Process analysis and sensitivity of ozone and particulate matter to precursor emissions. *Atmos. Environ.* 44, 3719-3727. 660 <https://doi.org/10.1016/j.atmosenv.2010.03.036>.
- Ming, L., Ling, J., Li, J., Fu, P., Yang, W., Di, L., Gan, Z., Wang, Z., and Li, X., 2017. PM2.5 in the Yangtze River Delta, China: Chemical compositions, seasonal variations, and regional pollution events. *Environ. Pollut.* 223, 200. <https://doi.org/10.1016/j.envpol.2017.01.013>.
- Nopmongcol, U., Koo, B., Tai, E., Jung, J., Piyachaturawat, P., Emery, C., Yarwood, G., Pirovano, G., Mitsakou, 665 C., and Kallos, G., 2012. Modeling Europe with CAMx for the Air Quality Model Evaluation International Initiative (AQMEII). *Atmos. Environ.* 53, 177-185. <https://doi.org/10.1016/j.atmosenv.2011.11.023>.
- Petäjä, T., Järvi, L., Kerminen, V. M., Ding, A. J., Sun, J. N., Nie, W., Kujansuu, J., Virkkula, A., Yang, X. Q., Fu, C. B., Zilitinkevich, S., and Kulmala, M., 2016. Enhanced air pollution via aerosol-boundary layer feedback in China. *Sci. Rep.* 6, 18998. <https://doi.org/10.1038/srep18998>. 670
- Pu, X., Wang, T. J., Huang, X., Melas, D., Zanis, P., Papanastasiou, D. K., and Poupkou, A., 2017. Enhanced surface ozone during the heat wave of 2013 in Yangtze River Delta region, China. *Sci. Total Environ.* 603-604, 807-816. <https://doi.org/10.1016/j.scitotenv.2017.03.056>.
- Qiao, X., Ying, Q., Li, X., Zhang, H., Hu, J., Tang, Y., and Chen, X., 2018. Source apportionment of PM2.5 for 25 Chinese provincial capitals and municipalities using a source-oriented Community Multiscale Air Quality model. *Sci. Total Environ.* 612, 462-471. <https://doi.org/10.1016/j.scitotenv.2017.08.272>. 675
- Quan, J., Gao, Y., Zhang, Q., Tie, X., Cao, J., Han, S., Meng, J., Chen, P., and Zhao, D., 2013. Evolution of planetary boundary layer under different weather conditions, and its impact on aerosol concentrations. *Particuology*. 11, 34-40. <https://doi.org/10.1016/j.partic.2012.04.005>.
- Rolph, G. D., 2013. Real-time Environmental Applications and Display sYstem (READY) Website. Silver Spring, MD: NOAA Air Resources Laboratory. ready. arl.noaa.gov.
- Sahu, L. K., Kondo, Y., Miyazaki, Y., Pongkiatkul, P., and Kim Oanh, N. T., 2011. Seasonal and diurnal 680 variations of black carbon and organic carbon aerosols in Bangkok. *J. Geophys. Res.* 116, D15302. <https://doi.org/10.1029/2010JD015563>.
- Seaton, A., MacNee, W., Donaldson, K., and Godden, D., 1995. Particulate air pollution and acute health effects. *Lancet*. 345, 176-178. [https://doi.org/10.1016/s0140-6736\(95\)90173-6](https://doi.org/10.1016/s0140-6736(95)90173-6). 685
- Shi, C., Wang, S., Liu, R., Zhou, R., Li, D., Wang, W., Li, Z., Cheng, T., and Zhou, B., 2015. A study of aerosol optical properties during ozone pollution episodes in 2013 over Shanghai, China. *Atmos. Res.* 153, 235-249. <https://doi.org/10.1016/j.atmosres.2014.09.002>.
- Shu, L., Xie, M., Wang, T., Gao, D., Chen, P., Han, Y., Li, S., Zhuang, B., and Li, M., 2016. Integrated studies of 690 a regional ozone pollution synthetically affected by subtropical high and typhoon system in the Yangtze River Delta region, China. *Atmos. Chem. Phys.* 16, 15801-15819. <https://doi.org/10.5194/acp-16-15801-2016>.
- Shu, L., Xie, M., Gao, D., Wang, T., Fang, D., Liu, Q., Huang, A., and Peng, L., 2017. Regional severe particle pollution and its association with synoptic weather patterns in the Yangtze River Delta region, China. *Atmos. Chem. Phys.* 17, 12871-12891. <https://doi.org/10.5194/acp-17-12871-2017>. 695
- State Environmental Protection Administration of China, 2006. China National Environmental Protection Standard: Automated Methods for Ambient Air Quality Monitoring, China Environmental Science Press, Beijing.
- Stein, A. F., Draxler, R. R., Rolph, G. D., Stunder, B. J. B., Cohen, M. D., and Ngan, F., 2015. NOAA's HYSPLIT Atmospheric Transport and Dispersion Modeling System. *Bull. Amer. Meteorol. Soc.* 96, 150504130527006.

- https://doi.org/10.1175/BAMS-D-14-00110.1.
- 700 Sun, Y., Wang, Z., Dong, H., Yang, T., Li, J., Pan, X., Chen, P., and Jayne, J. T., 2012. Characterization of summer organic and inorganic aerosols in Beijing, China with an Aerosol Chemical Speciation Monitor. *Atmos. Environ.* 51, 250-259. https://doi.org/10.1016/j.atmosenv.2012.01.013.
- Vautard, R., Menut, L., Beekmann, M., Chazette, P., Flamant, P. H., Gombert, D., Guédalia, D., Kley, D., Lefebvre, M.-P., Martin, D., Mégie, G., Perros, P., and Toupane, G., 2003. A synthesis of the Air Pollution Over the Paris Region (ESQUIF) field campaign. *J. Geophys. Res.* 108, 8558. https://doi.org/10.1029/2003JD003380.
- 705 Wagstrom, K. M., Pandis, S. N., Yarwood, G., Wilson, G. M., and Morris, R. E., 2008. Development and application of a computationally efficient particulate matter apportionment algorithm in a three-dimensional chemical transport model. *Atmos. Environ.* 42, 5650-5659. https://doi.org/10.1016/j.atmosenv.2008.03.012.
- 710 Wang, F., Guo, Z., Lin, T., and Rose, N. L., 2016. Seasonal variation of carbonaceous pollutants in PM2.5 at an urban 'supersite' in Shanghai, China. *Chemosphere.* 146, 238-244. https://doi.org/10.1016/j.chemosphere.2015.12.036.
- Wang, J., Wang, S., Jiang, J., Ding, A., Zheng, M., Zhao, B., Wong, D. C., Zhou, W., Zheng, G., and Wang, L., 2014. Impact of aerosol-meteorology interactions on fine particle pollution during China's severe haze episode in January 2013. *Environ. Res. Lett.* 9, 094002. https://doi.org/10.1088/1748-9326/9/9/094002.
- 715 Wang, T. J., Lam, K. S., Xie, M., Wang, X. M., Carmichael, G., and Li, Y. S., 2006. Integrated studies of a photochemical smog episode in Hong Kong and regional transport in the Pearl River Delta of China. *Tellus Ser. B-Chem. Phys. Meteorol.* 58, 31-40. https://doi.org/10.1111/j.1600-0889.2005.00172.x.
- Wang, T., Xue, L., Brimblecombe, P., Lam, Y. F., Li, L., and Zhang, L., 2017. Ozone pollution in China: A review 720 of concentrations, meteorological influences, chemical precursors, and effects. *Sci. Total Environ.* 575, 1582-1596. https://doi.org/10.1016/j.scitotenv.2016.10.081.
- Wang, X., Wang, W., Yang, L., Gao, X., Nie, W., Yu, Y., Xu, P., Zhou, Y., and Wang, Z., 2012. The secondary formation of inorganic aerosols in the droplet mode through heterogeneous aqueous reactions under haze conditions. *Atmos. Environ.* 63, 68-76. https://doi.org/10.1016/j.atmosenv.2012.09.029.
- 725 Wang, Y., Zhuang, G., Tang, A., Yuan, H., Sun, Y., Chen, S., and Zheng, A., 2005. The ion chemistry and the source of PM2.5 aerosol in Beijing. *Atmos. Environ.* 39, 3771-3784. https://doi.org/10.1016/j.atmosenv.2005.03.013.
- Wang, Y., Bao, S., Wang, S., Hu, Y., Shi, X., Wang, J., Zhao, B., Jiang, J., Zheng, M., Wu, M., Russell, A. G., Wang, Y., and Hao, J., 2017. Local and regional contributions to fine particulate matter in Beijing during 730 heavy haze episodes. *Sci. Total Environ.* 580, 283-296. https://doi.org/10.1016/j.scitotenv.2016.12.127.
- Wu, D., Fung, J. C. H., Yao, T., and Lau, A. K. H., 2013a. A study of control policy in the Pearl River Delta region by using the particulate matter source apportionment method. *Atmos. Environ.* 76, 147-161. https://doi.org/10.1016/j.atmosenv.2012.11.069.
- 735 Wu, M., Wu, D., Fan, Q., Wang, B. M., Li, H. W., and Fan, S. J., 2013b. Observational studies of the meteorological characteristics associated with poor air quality over the Pearl River Delta in China. *Atmos. Chem. Phys.* 13, 10755-10766. https://doi.org/10.5194/acp-13-10755-2013.
- Xie, M., Shu, L., Wang, T.-j., Liu, Q., Gao, D., Li, S., Zhuang, B.-l., Han, Y., Li, M.-m., and Chen, P.-l., 2017. Natural emissions under future climate condition and their effects on surface ozone in the Yangtze River Delta region, China. *Atmos. Environ.* 150, 162-180. https://doi.org/10.1016/j.atmosenv.2016.11.053.
- 740 Xie, M., Wang, T.J., Jiang, F., Yang, X.Q., 2007. Modeling of natural NO_x and VOC emissions and their effects

- on tropospheric photochemistry in China. *Environ. Sci.* 28, 31-40.
- Xie, M., Zhu, K. G., Wang, T. J., Yang, H. M., Zhuang, B. L., Li, S., Li, M. G., Zhu, X. S., and Ouyang, Y., 2014. Application of photochemical indicators to evaluate ozone nonlinear chemistry and pollution control countermeasure in China, *Atmos. Environ.* 99, 466–473. <https://doi.org/10.1016/j.atmosenv.2014.10.013>.
- 745 Xie, M., Zhu, K., Wang, T., Chen, P., Han, Y., Li, S., Zhuang, B., and Shu, L., 2016. Temporal characterization and regional contribution to O₃ and NO_x at an urban and a suburban site in Nanjing, China. *Sci. Total Environ.* 551-552, 533-545. <https://doi.org/10.1016/j.scitotenv.2016.02.047>.
- Yarwood, G., Morris, R., Yocke, M., Hogo, H., and Chico, T., 1996. Development of a methodology for source apportionment of ozone concentration estimates from a photochemical grid model. *J. Air Waste Manage.* 750 Assoc. PITTSBURGH, PA 15222(USA).[np].
- Yarwood, G., Rao, S., Yocke, M., and Z. Whitten, G., 2005. Updates to the Carbon Bond Mechanism: CB05. Final report to the US EPA, RT-0400675, 8. http://www.camx.com/publ/pdfs/CB05_Final_Report_120805.pdf.
- Yarwood G., Morris R.E., and Wilson G.M., 2007. Particulate Matter Source Apportionment Technology (PSAT) in the CAMx Photochemical Grid Model. In: Borrego C., Norman AL. (eds) Air Pollution Modeling and Its Application XVII. Springer, Boston, MA. https://doi.org/10.1007/978-0-387-68854-1_52.
- Ying, Q., Wu, L., Zhang, H., 2014. Local and inter-regional contributions to PM_{2.5} nitrate and sulfate in China. *Atmos. Environ.* 94, 582-592. <https://doi.org/10.1016/j.atmosenv.2014.05.078>.
- Zhang, L., Brook, J. R., and Vet, R., 2003. A revised parameterization for gaseous dry deposition in air-quality models. *Atmos. Chem. Phys.* 3, 2067-2082. <https://doi.org/10.5194/acp-3-2067-2003>.
- 760 Zhang, Y. H., Hu, M., Zhong, L. J., Wiedensohler, A., Liu, S. C., Andreae, M. O., Wang, W., and Fan, S. J., 2008. Regional Integrated Experiments on Air Quality over Pearl River Delta 2004 (PRIDE-PRD2004): Overview. *Atmos. Environ.* 42, 6157-6173. <https://doi.org/10.1016/j.atmosenv.2008.03.025>.
- Zhang, H., Wang, S., Hao, J., Wang, X., Wang, S., Chai, F., and Li, M., 2016. Air pollution and control action in Beijing. *J. Clean. Prod.* 112, 1519-1527. <https://doi.org/10.1016/j.jclepro.2015.04.092>.
- 765 Zheng, G. J., Duan, F. K., Su, H., Ma, Y. L., Cheng, Y., Zheng, B., Zhang, Q., Huang, T., Kimoto, T., Chang, D., Pöschl, U., Cheng, Y. F., and He, K. B., 2015. Exploring the severe winter haze in Beijing: the impact of synoptic weather, regional transport and heterogeneous reactions. *Atmos. Chem. Phys.* 15, 2969-2983. <https://doi.org/10.5194/acp-15-2969-2015>.
- 770

Table and Figure

Table 1. The grid setting and configurations of the CAMx model.

Items	Options
Dimensions (x, y) in WRF	(74,98), (100,112)
Dimensions (x, y) in CAMx	(74,98), (95, 107)
Grid spacing (km)	27, 9
Horizontal advection solver	Piecewise Parabolic Method (PPM)
Vertical advection solver	Implicit backward-Euler hybrid
Vertical diffusion	K-theory
Dry Deposition	Zhang et al., 2003
Gas-Phase chemistry	Carbon Bond chemistry (CB05) (Yarwood et al., 2005)
Chemistry solver	Euler-Backward Iterative (EBI)
Particulate matter chemistry	a static two-mode coarse/fine (CF) scheme

775 **Table 2.** The comparison of observed and simulated SOR and NOR (average over PD, DSL, ZH
and CCM sites) during different episodes of the CAPUM-YRD in 2016.

	PM25_Ep1	PM25_Ep2	PM25_Clean	O3_Ep1	O3_Ep2	O3_Ep3	O3_Clean
SOR	Obs. ^a 0.281±0.046	0.262±0.060	0.197±0.058	0.251±0.081	0.387±0.056	0.389±0.046	0.359±0.071
	Sim. ^b 0.069±0.016	0.071±0.020	0.067±0.006	0.077±0.020	0.067±0.018	0.076±0.020	0.086±0.029
NOR	Obs. ^a 0.180±0.059	0.169±0.073	0.101±0.061	0.068±0.021	0.101±0.055	0.153±0.062	0.105±0.055
	Sim. ^b 0.066±0.056	0.046±0.021	0.040±0.017	0.047±0.030	0.036±0.036	0.051±0.041	0.042±0.030

^a Calculated using observed SO₂, NO₂, SO₄²⁻ and NO₃⁻ data;

^b Calculated using simulated SO₂, NO₂, SO₄²⁻ and NO₃⁻ concentrations contributed by local emission obtained from PSAT results.

780

Table 3. Comparison of OC, EC and OC/EC between different YRD cities.

Cities	Site description	Season	Sampling period	OC ($\mu\text{g}/\text{m}^3$)	EC ($\mu\text{g}/\text{m}^3$)	OC/EC Reference
Shanghai (PD)	Suburban	—	Aug-Sep 2016	3.7	0.8	5.1
			Nov-Dec 2016	10.2	3.8	3.1
Shanghai (DSL)	Rural	—	Aug-Sep 2016	5.9	1.3	5.0
			Nov-Dec 2016	8.4	3.5	2.9
Nanjing (CCM)	Urban	—	Aug-Sep 2016	7.8	3.6	2.1
			Nov-Dec 2016	8.0	4.9	1.7
Shanghai	Urban	Autumn	Oct-Nov 2011	7.9	3.1	2.4
		Winter	Dec 2011-Jan 2012	9.6	3.8	2.7
		Spring	Apr 2012	7.6	2.7	2.8
		Summer	Jul-Aug 2012	5.3	2.0	3.2
Shanghai	Urban	Autumn	Oct-Nov 2013	7.0	1.0	7.4
		Winter	Dec 2013-Jan 2014	17.2	2.9	6.9
		Spring	Mar-Apr 2014	7.5	1.3	6.4
		Summer	Jun-Jul 2014	4.9	0.8	6.0
Nanjing	Urban	Autumn	Nov 2011	15.7	5.9	2.8
		Spring	Mar 2012	8.5	3.8	2.3
		Summer	Jun 2012	7.6	3.1	2.5
		Winter	Dec 2013-Feb 2014	22.5	8.2	2.7
Nanjing	Suburban	Summer	Jun–Aug 2013	6.5	4.1	1.6
		Summer	Jun–Aug 2014	4.3	2.5	1.7
		Autumn	Sep–Nov 2013	11.0	5.4	2.0
		Autumn	Sep–Nov 2014	4.0	2.5	1.6
Lin'an	Background site	Winter	Dec 2013–Feb 2014	11.6	6.0	1.9
		Winter	Dec 2014–Feb 2015	8.0	4.4	1.8
		Spring	Mar–May 2014	6.6	3.4	1.9
		Spring	Mar–May 2015	8.0	2.8	2.8
Ningbo	Urban(4), Suburban(1)	—	Dec 2012-Nov 2013	7.0~12.9	1.58~4.1	2.9~4.2 Li et al., 2017a

785

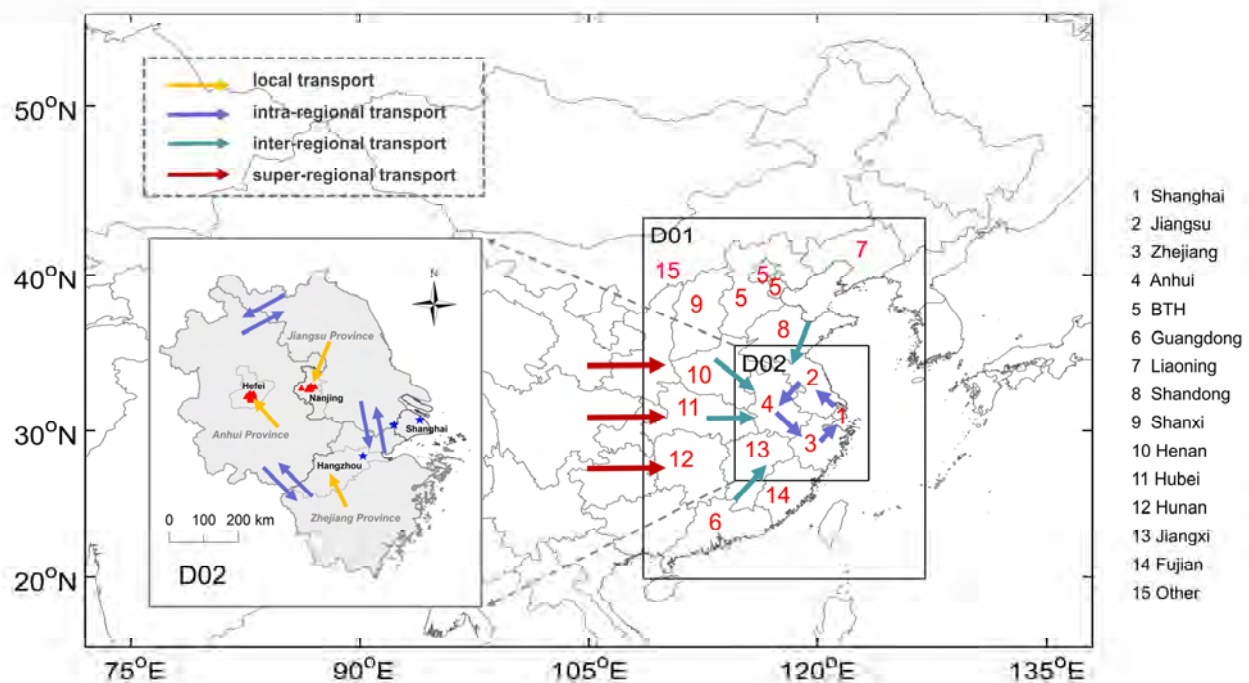


Figure 1. The 27-, 9-km domains and subdivided source regions applied in the CAMx simulation.

The blue star and red triangle symbols show the locations of super and national monitoring sites in YRD, respectively. The arrows in different colors represent the diverse spatial scales of transport.

790 The super-regional transport represents the transport across the boundaries of the two-nested domain (BTH: Beijing-Tianjin-Hebei; Other: the rest of the study domain excluding 14 regions).

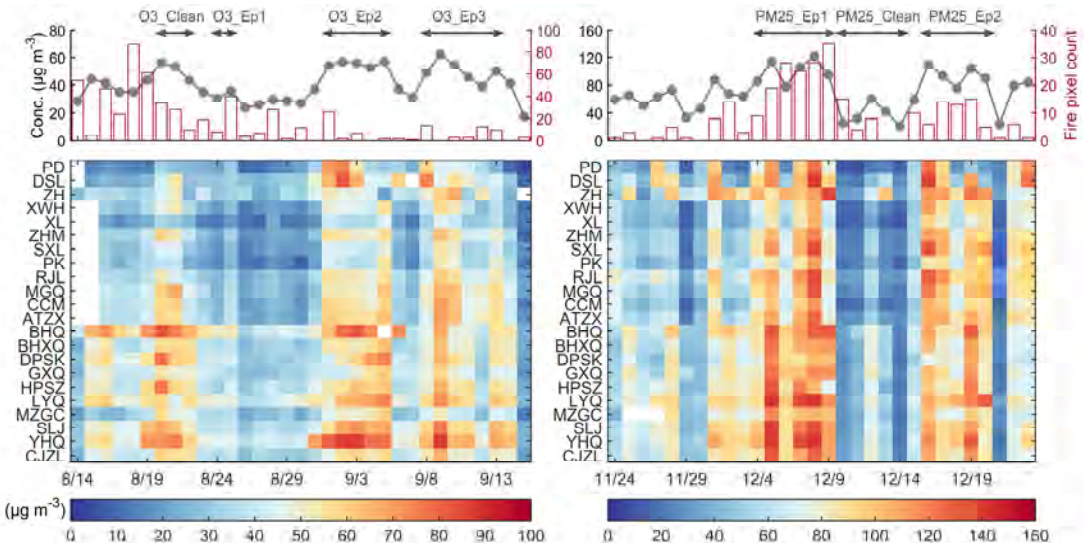


Figure 2. Day-to-day variation of daily average $\text{PM}_{2.5}$ concentrations at 22 sites in YRD during

the summer (left panel) and winter (right panel) experiments of the CAPUM-YRD in 2016. The gray solid dot line indicates the regional average $\text{PM}_{2.5}$ over 22 sites. The red column shows the daily MODIS fire counts at greater than 50% confidence interval in box D02 (Fig. 1). Site information is listed in Table S1. Note the different magnitude of the values in winter and summer.

800

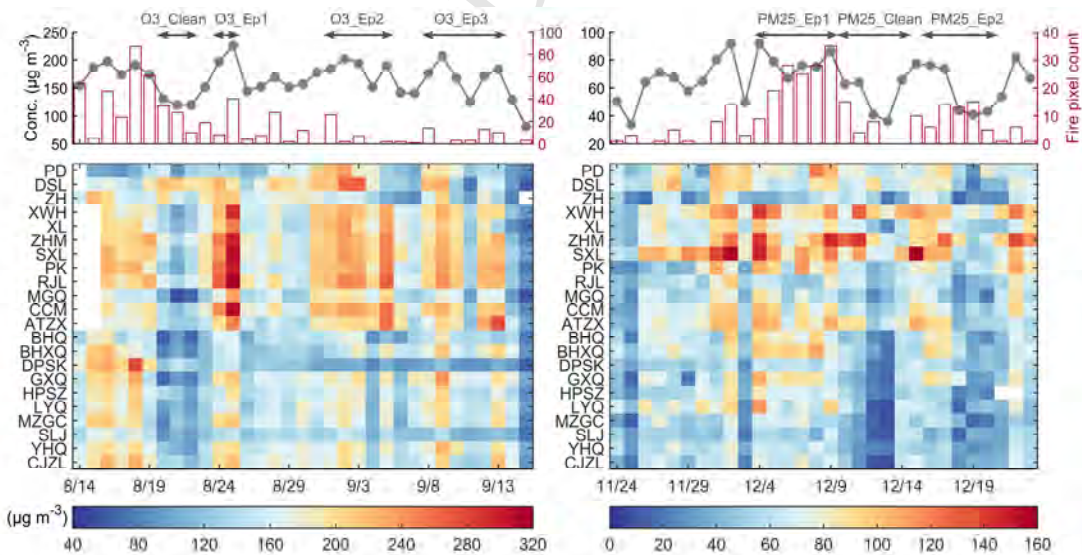


Figure 3. As in Fig. 2, but for MDA8 O_3 .

805

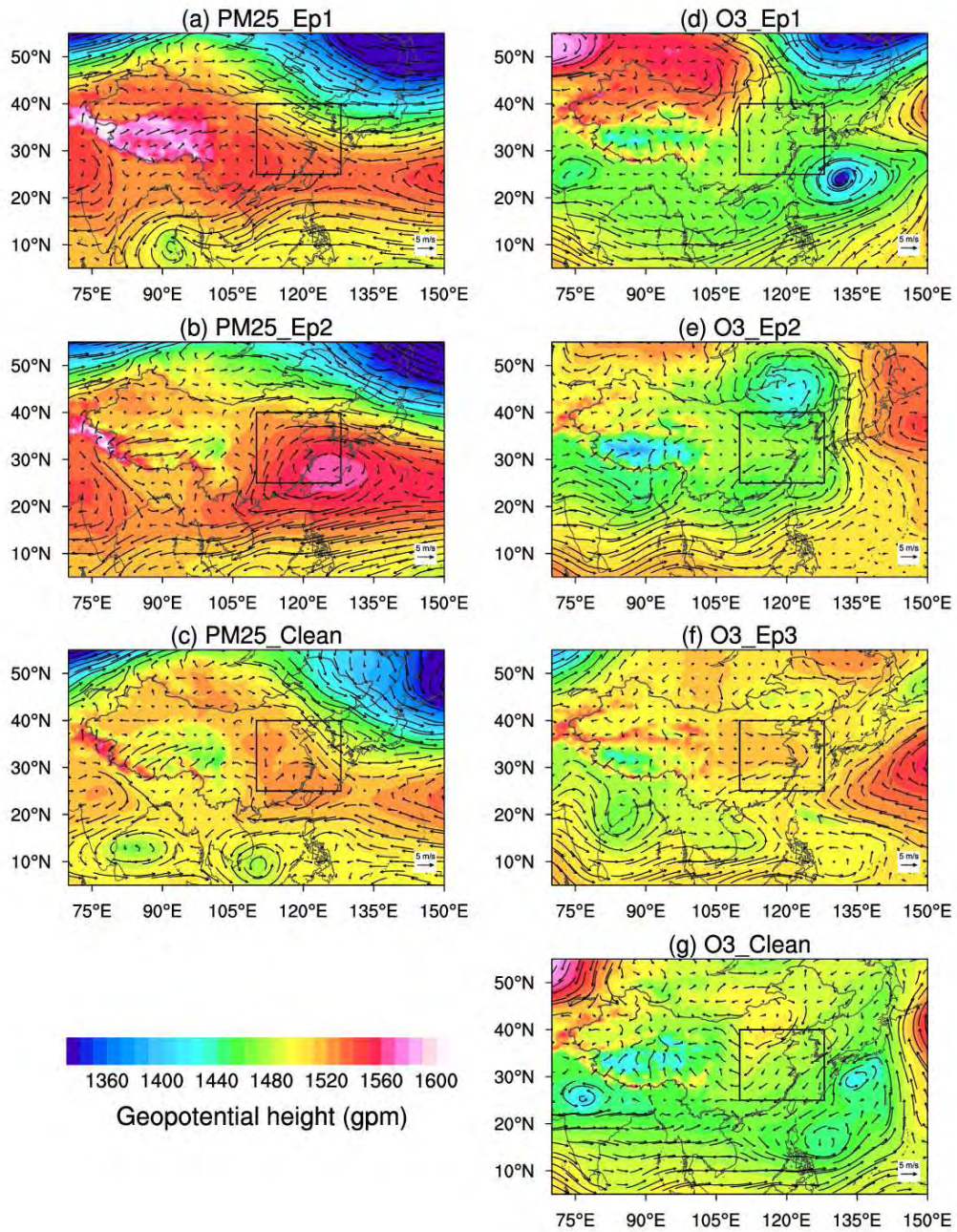
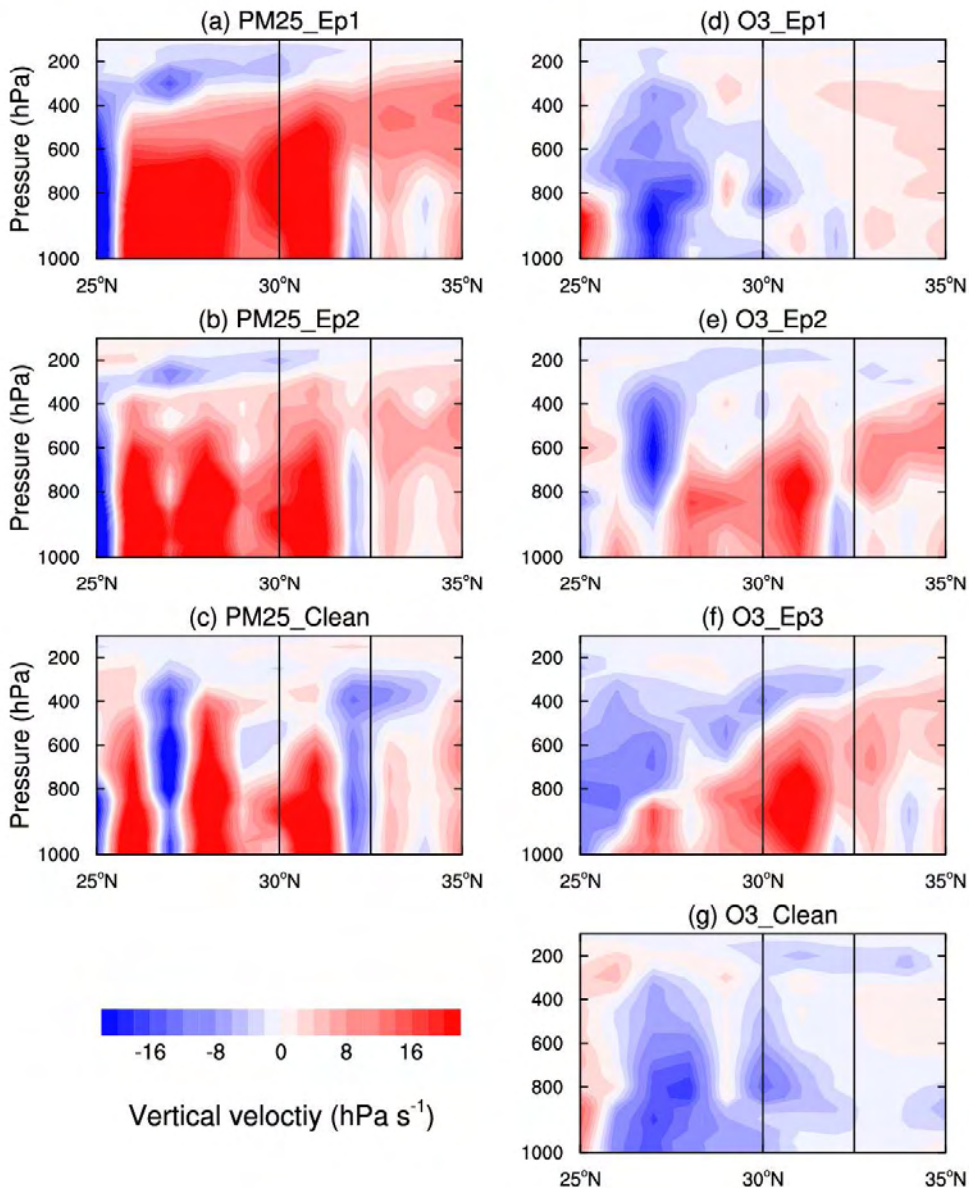


Figure 4. Average geopotential height field and wind field at 850 hPa during different PM_{2.5} (**a-c**) and O₃ (**d-g**) episodes of the CAPUM-YRD in 2016. The boxed area highlights the domain of 25-40°N, 110-128°E.



810

Figure 5. Height-latitude cross-section of vertical velocity averaged over the longitude of 117-122°E during different PM_{2.5} (**a-c**) and O₃ (**d-g**) episodes of the CAPUM-YRD in 2016. All monitoring sites in YRD are located within the latitude of 30-32.5°N (boxed area). Positive (negative) values indicate downward (upward) atmospheric motions.

815

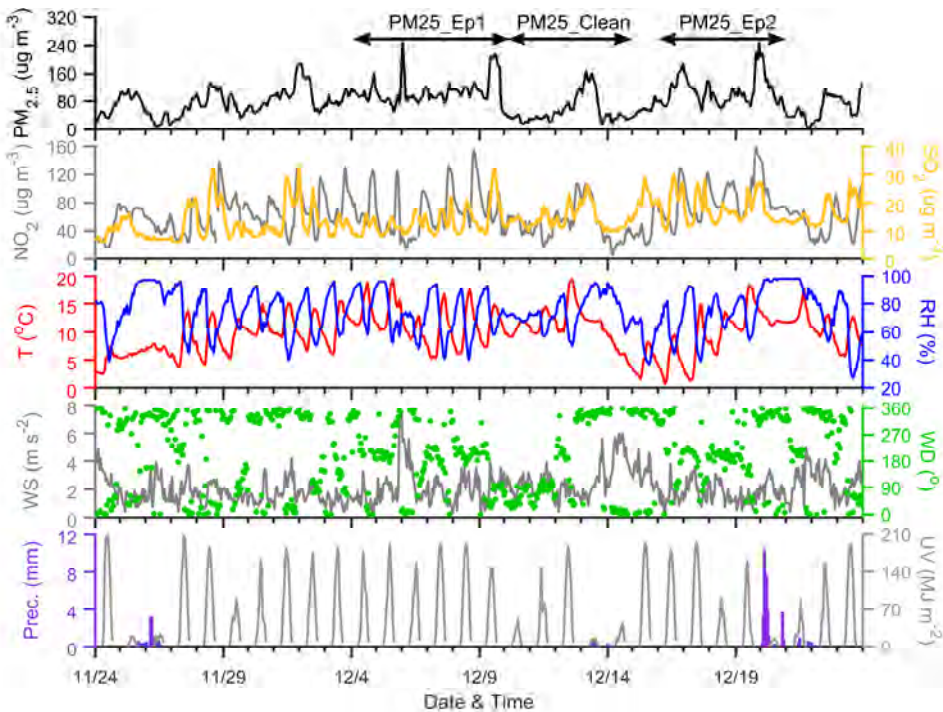


Figure 6. Temporal variation of main air pollutants and meteorological parameters in Hangzhou during the winter experiment of the CAPUM-YRD in 2016. The concentrations of air pollutants are obtained from ZH site. The meteorological data are obtained from Hangzhou weather station

820 (120.1667°E, 30.2333°N).

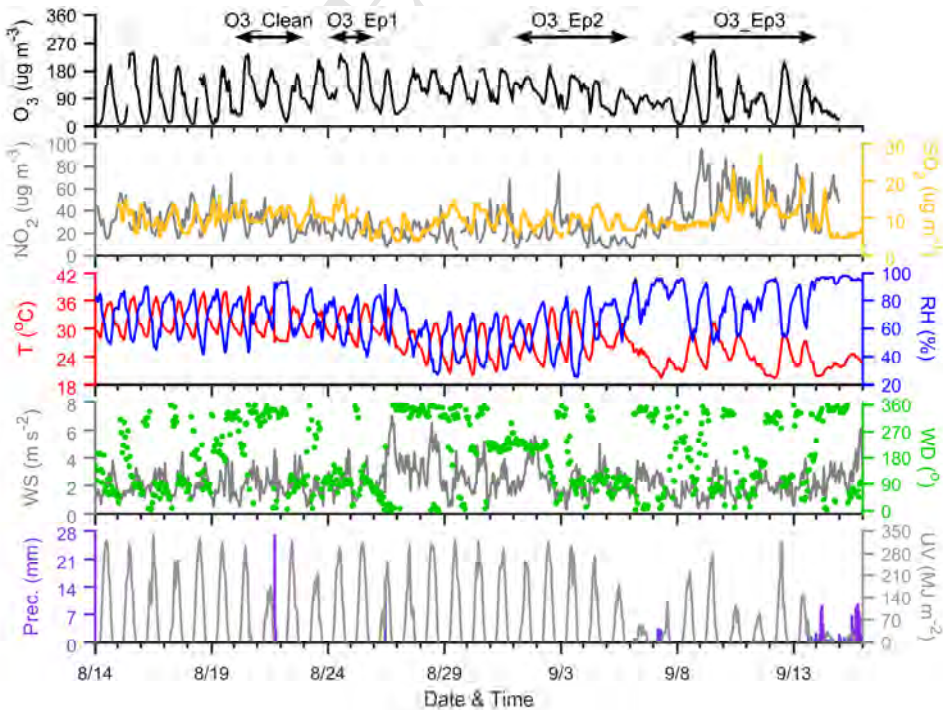
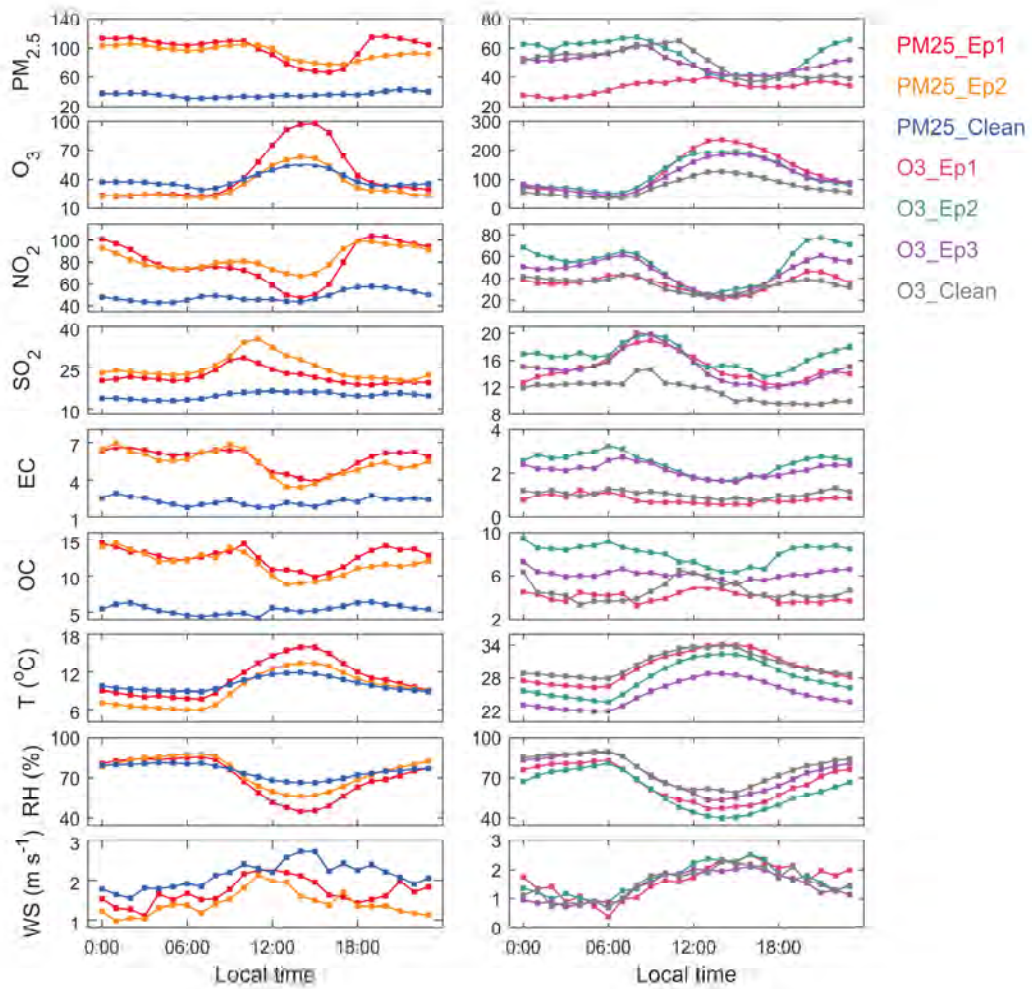


Figure 7. As in Fig. 6, but for the summer experiment.



825 **Figure 8.** The diurnal variation of main air pollutants (PM_{2.5}, O₃, NO₂, SO₂: averaged over 22 sites; EC, OC: averaged over PD, DSL and CCM sites; unit: $\mu\text{g}/\text{m}^3$) and meteorological parameters (averaged over Pudong, Hangzhou and Xianlin weather stations) during different PM_{2.5} (left panel) and O₃ (right panel) episodes of the CAPUM-YRD in 2016. Vertical bars denote one standard deviation over the sites.

830

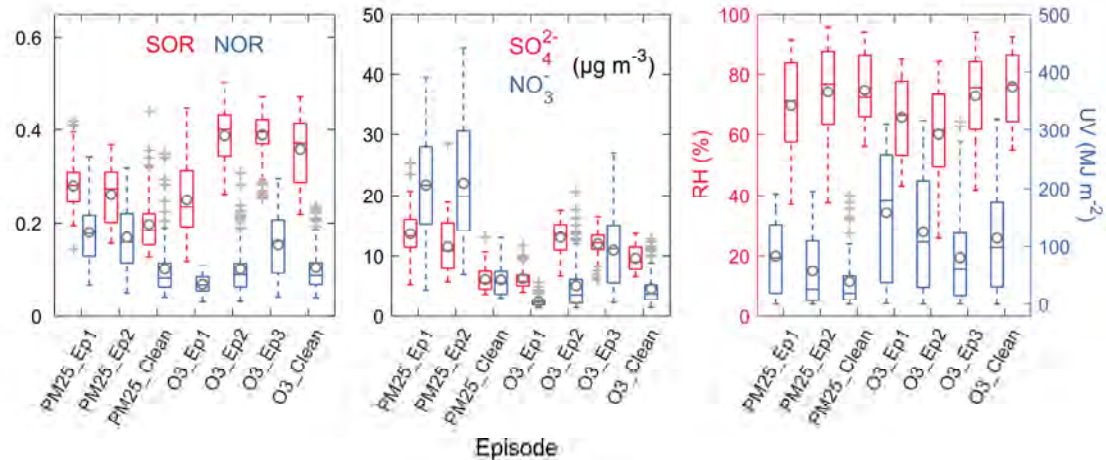


Figure 9. The box-and-whisker plot of SOR, NOR, SO_4^{2-} and NO_3^- (PD, DSL, ZH and CCM sites), as well as RH (Pudong, Hangzhou and Xianlin weather stations) and net radiation

(Hangzhou weather station), during different episodes of the CAPUM-YRD in 2016. Box

835 boundaries represent the interquartile range, bars represent 5%-95% percentile range, horizontal
lines represent the median value, and gray hollow circles represent the average value.

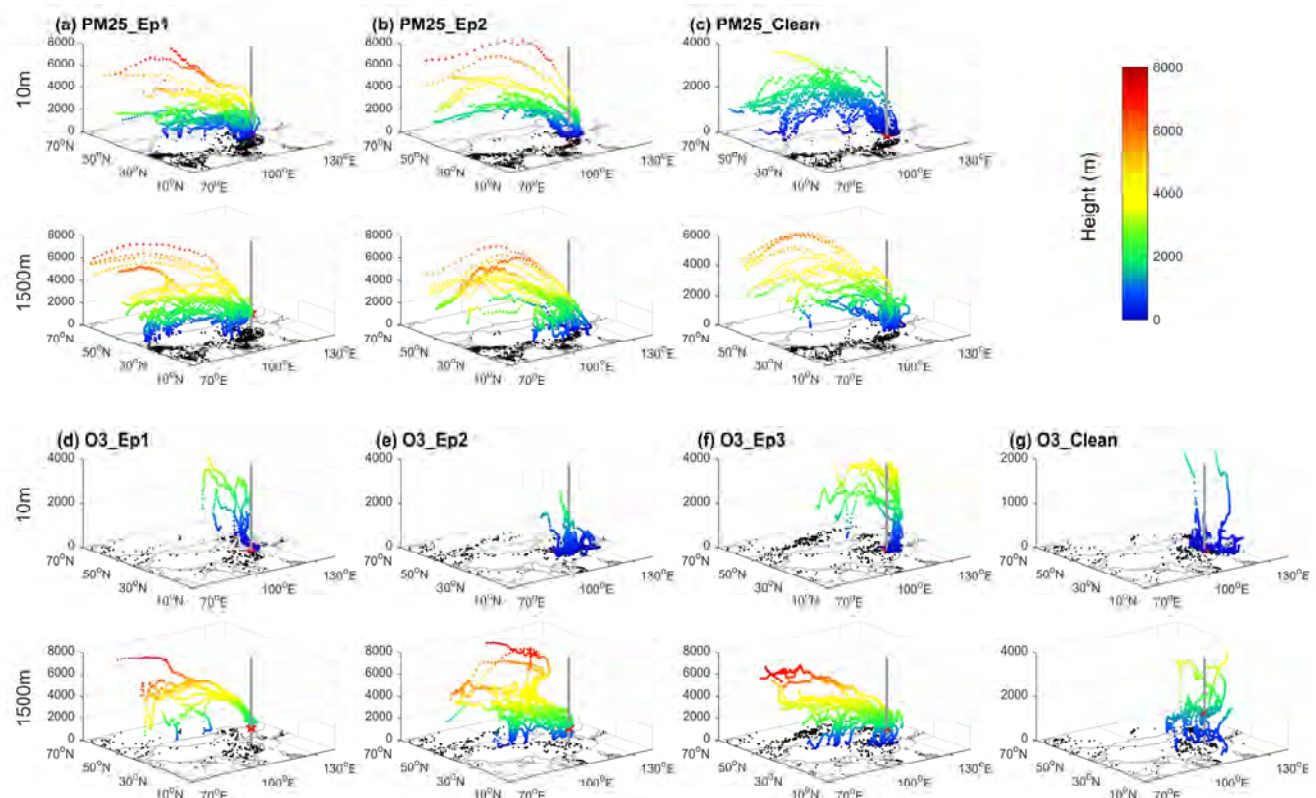


Figure 10. 144-h backward trajectories ending at a height of 10 m and 1500 m, as well as MODIS fire counts at greater than 50% confidence interval, during different PM_{2.5} (**a-c**) and O₃ (**d-g**) episodes of the CAPUM-YRD in 2016. The red star and bold grey line indicate the location of CCM site (118.75°E, 32.06°N) in Nanjing.

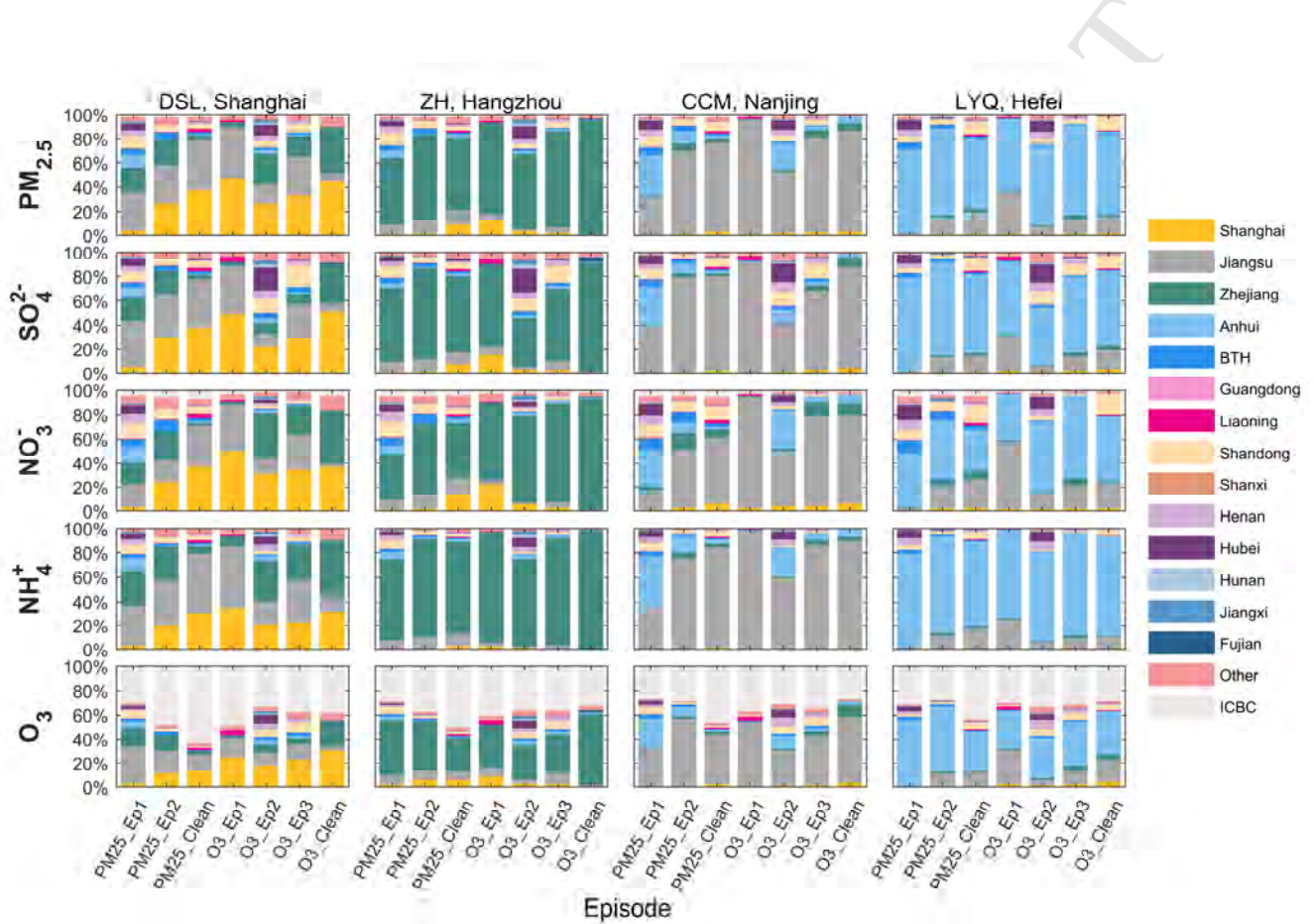
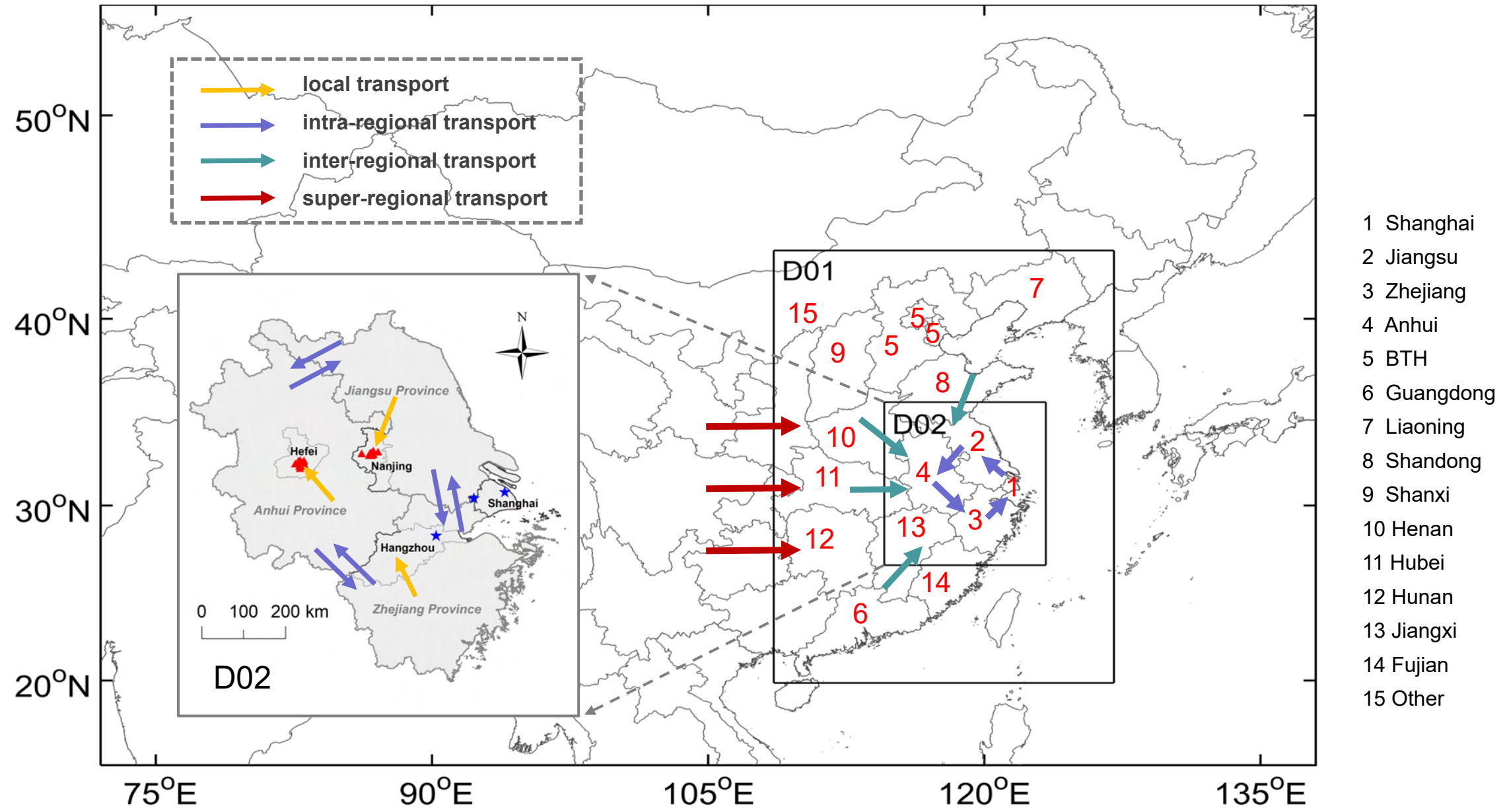
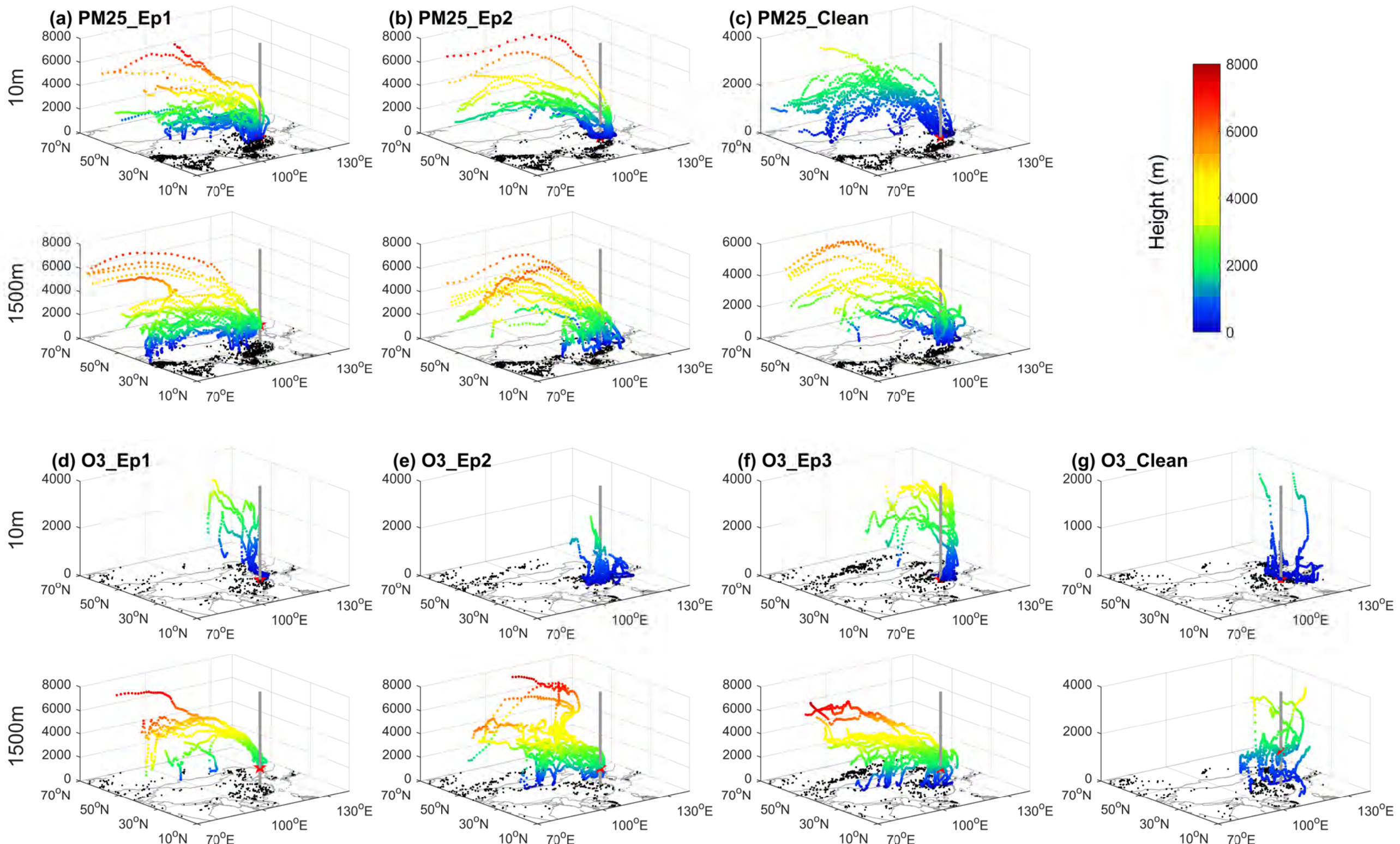
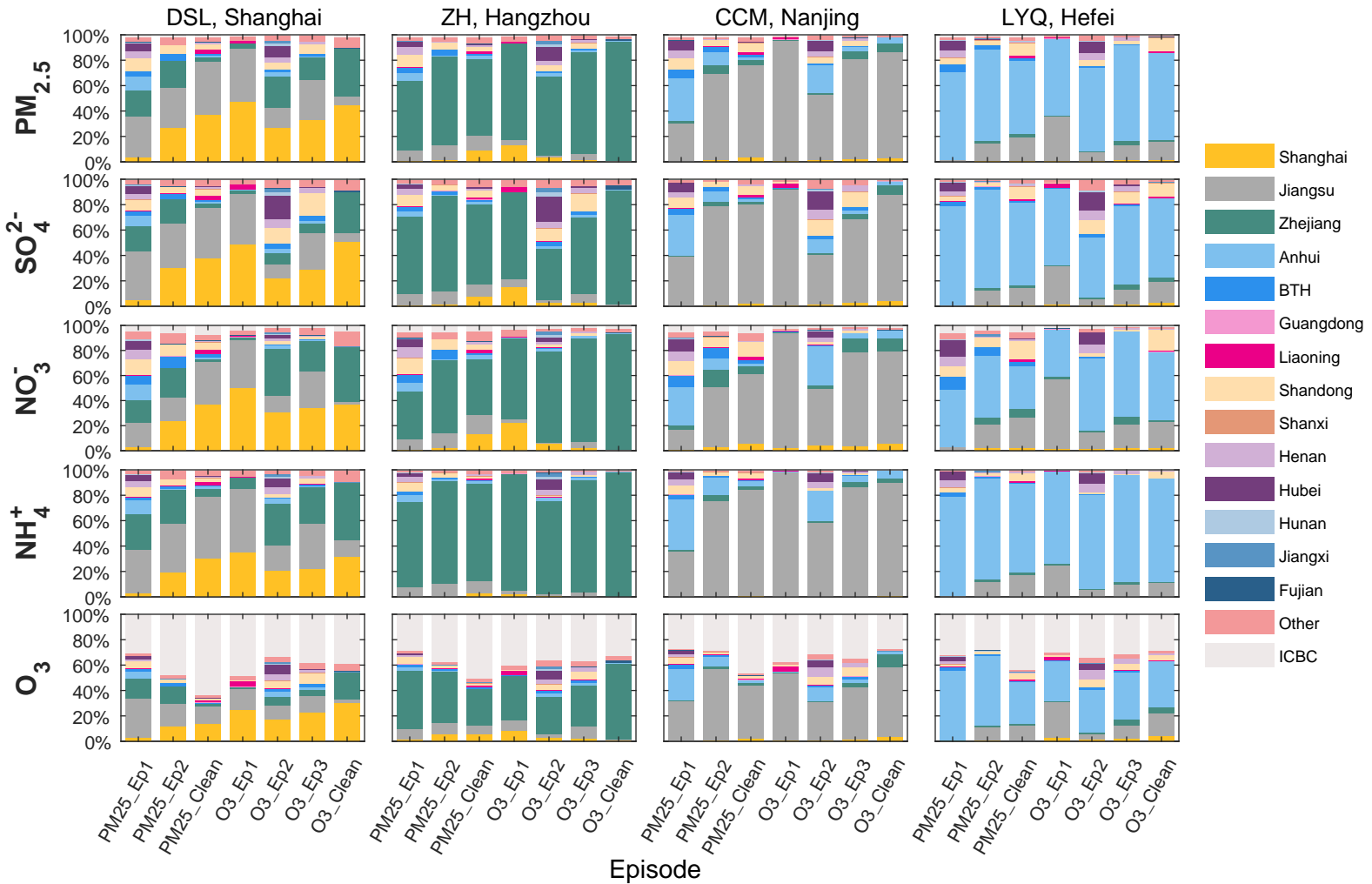
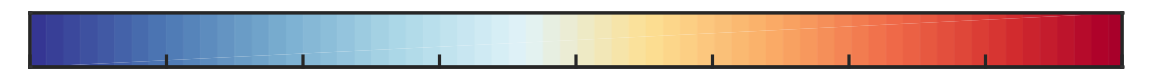
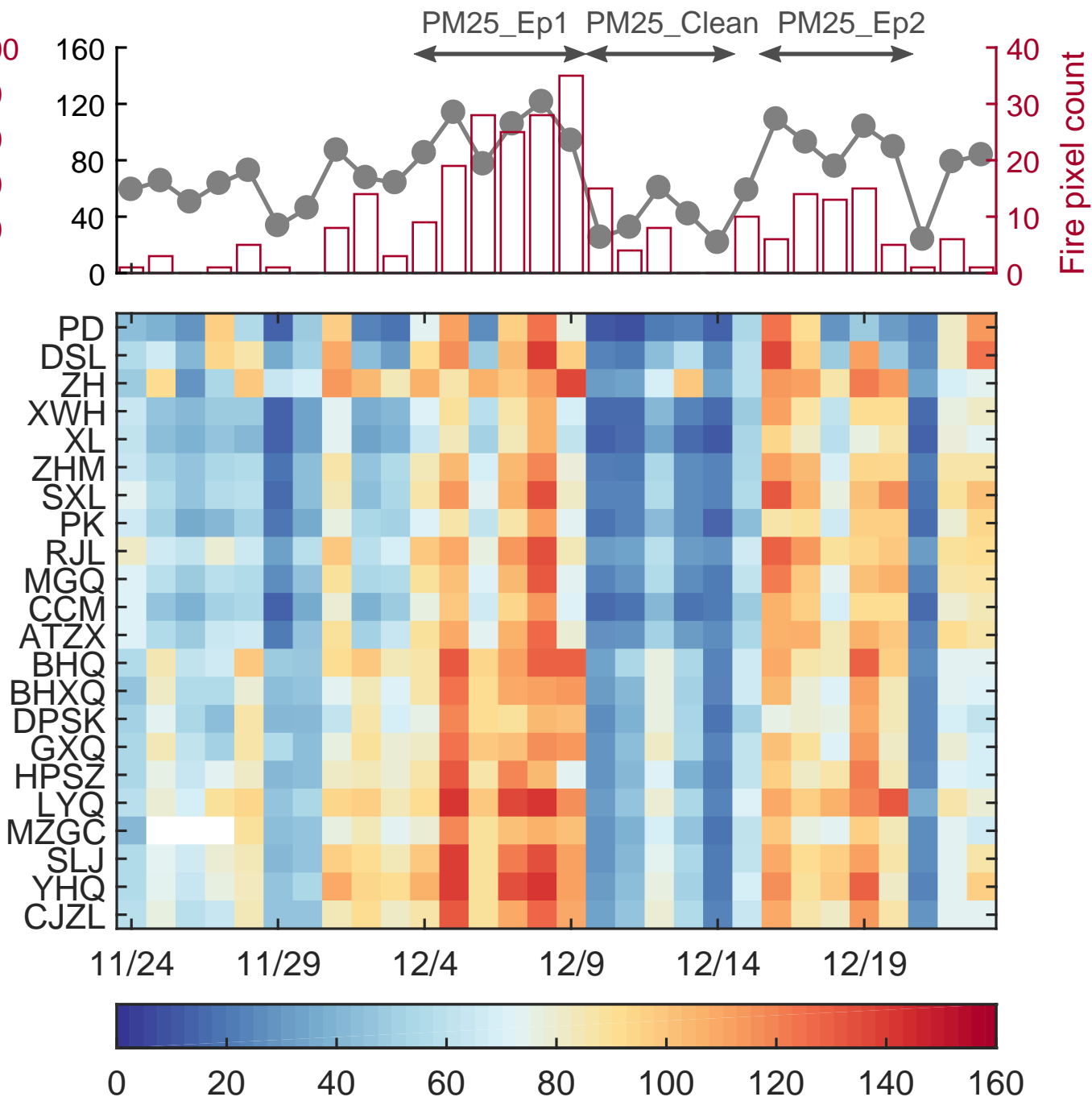
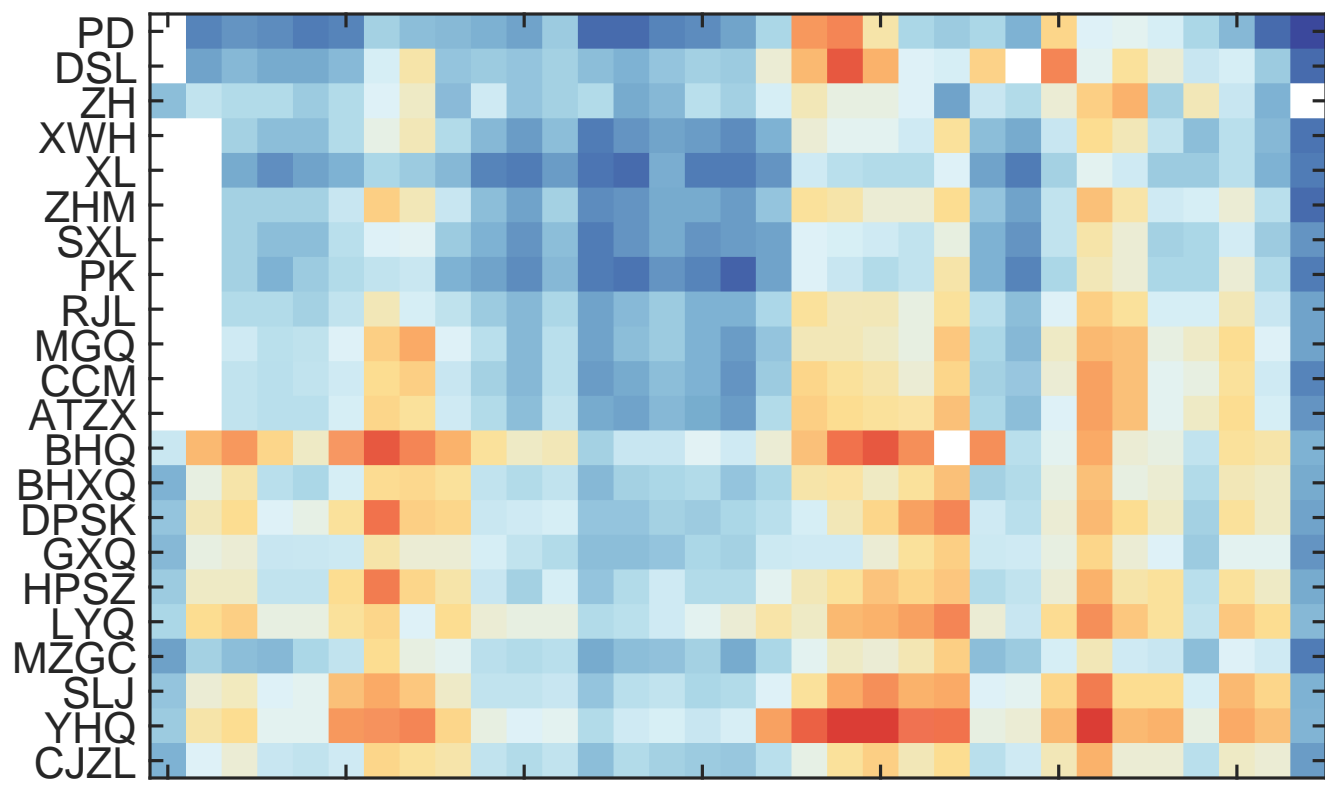
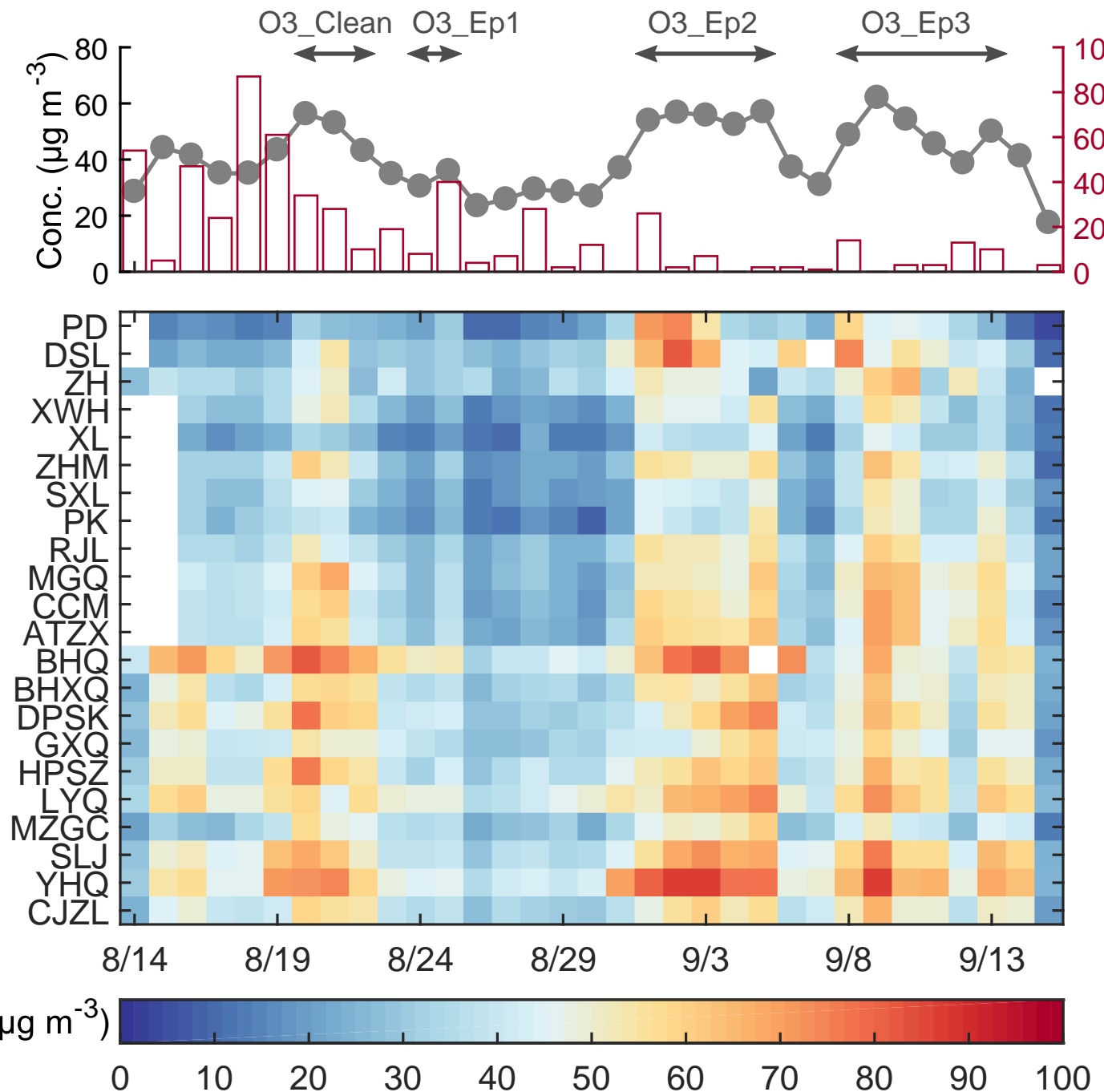


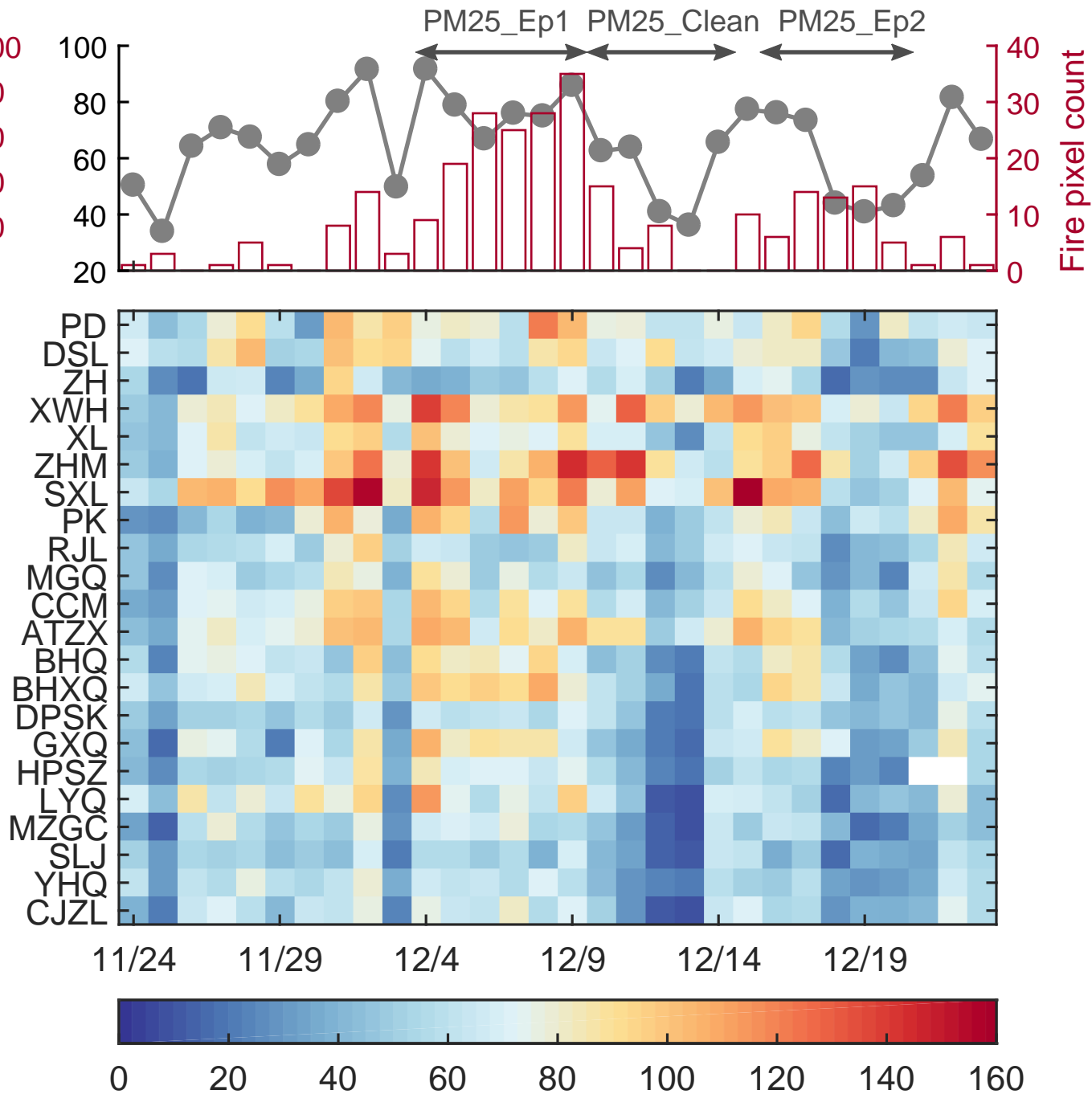
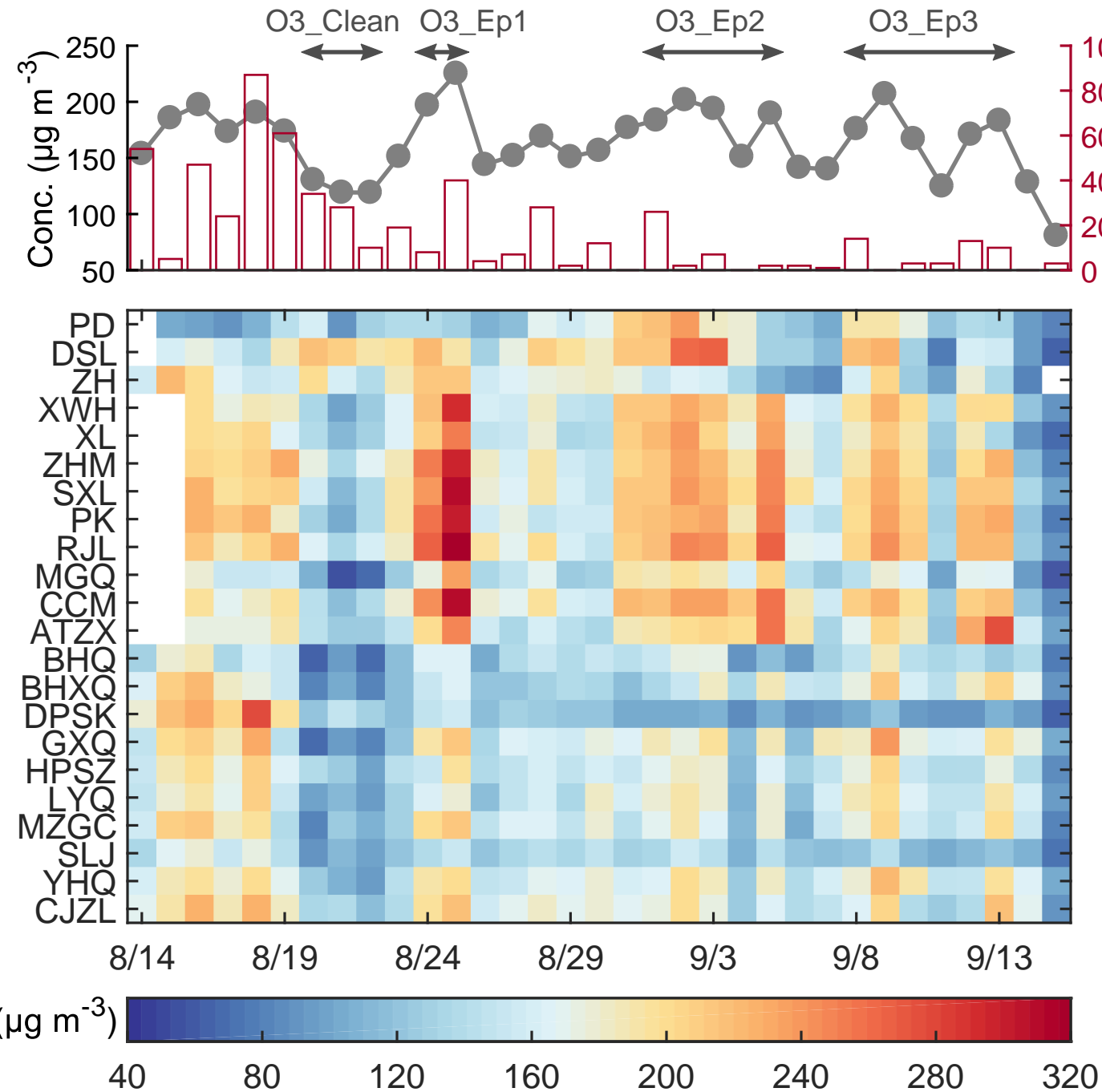
Figure 11. Average source region contributions to PM_{2.5}, inorganic components of PM_{2.5} (SO₄²⁻, NO₃⁻ and NH₄⁺) and daytime O₃ concentrations of DSL, ZH, CCM and LYQ sites during different episodes of the CAPUM-YRD in 2016 (BTH: Beijing-Tianjin-Hebei; Other: the rest of the study domain excluding 14 regions; ICBC: initial and boundary conditions).

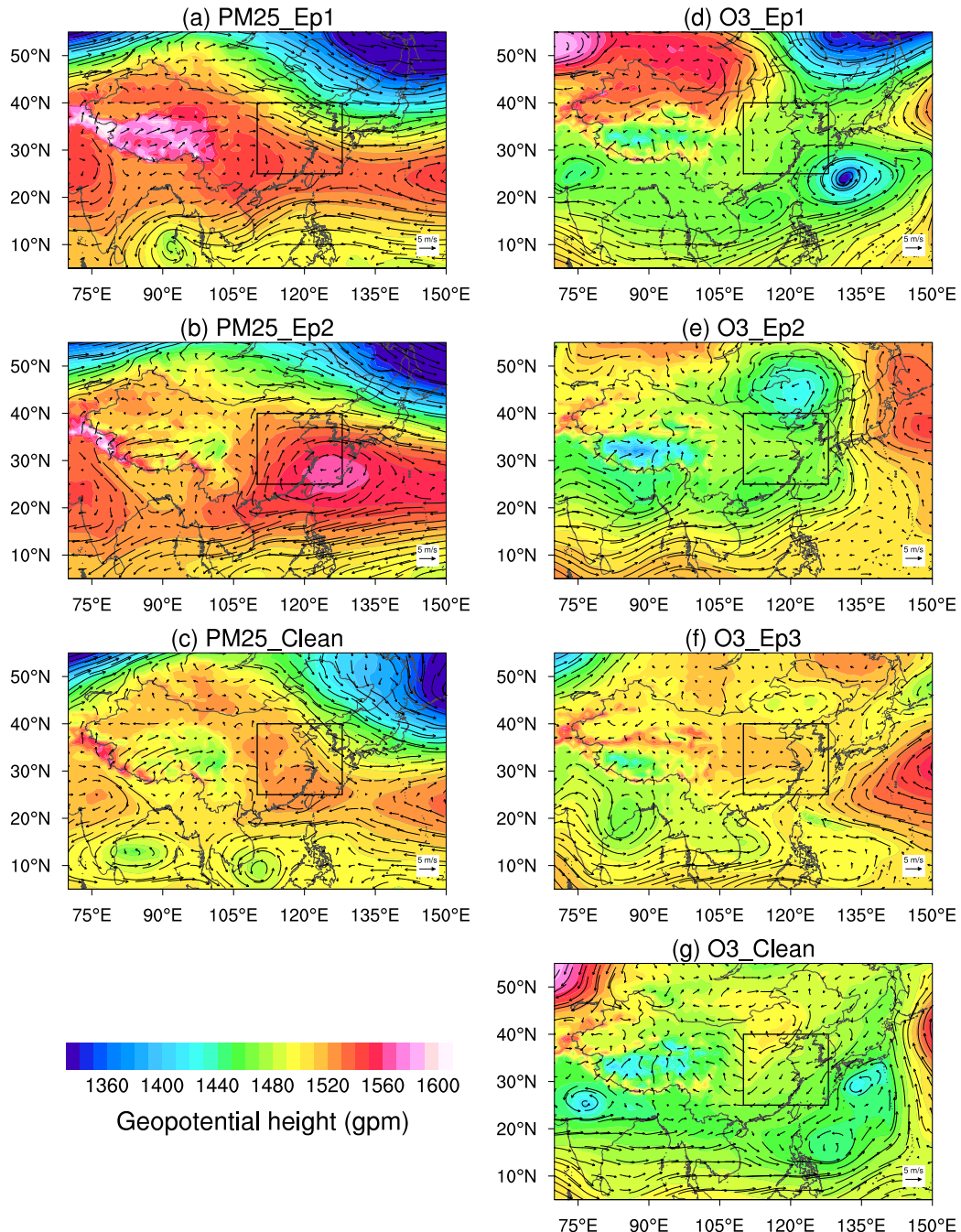


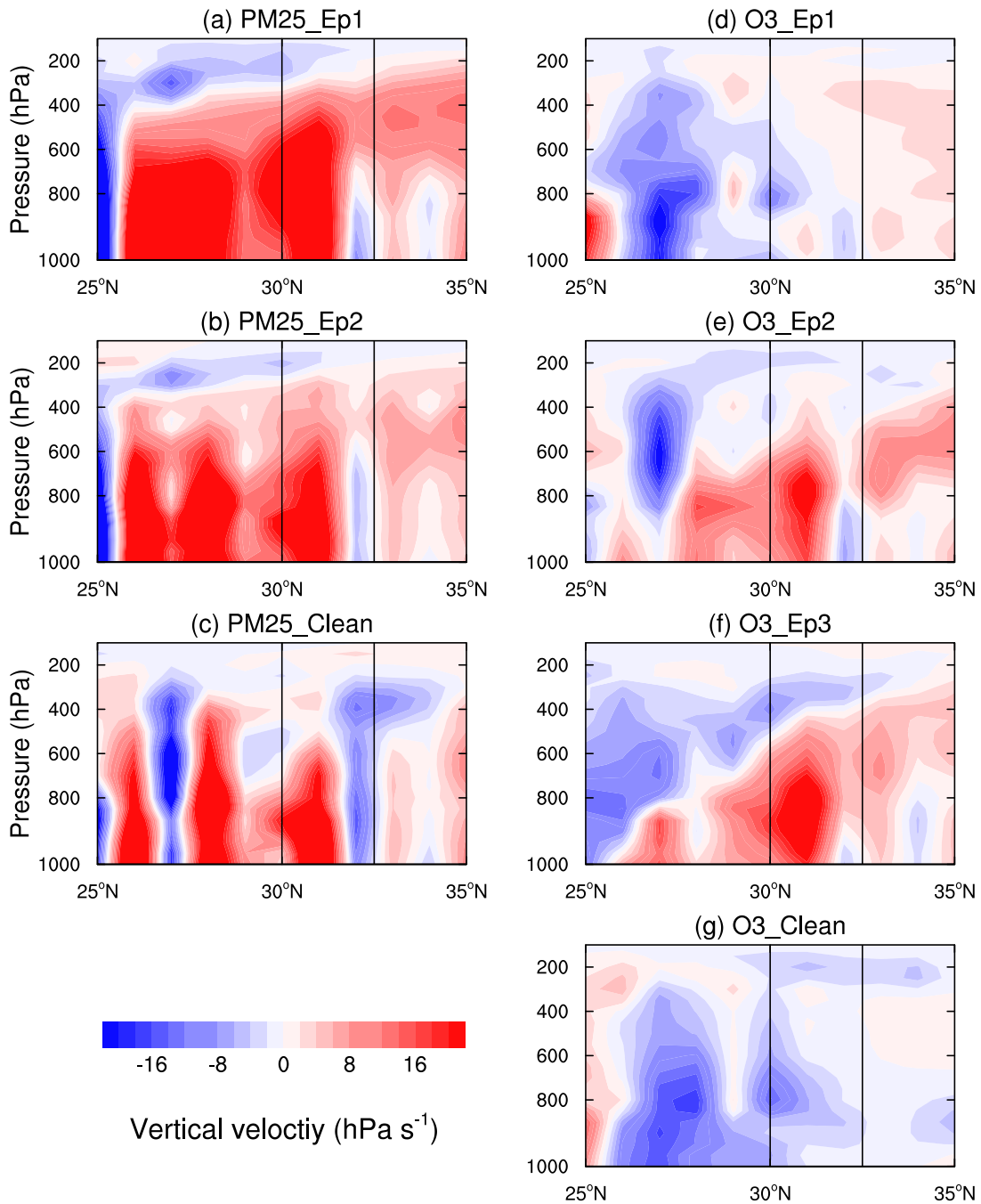


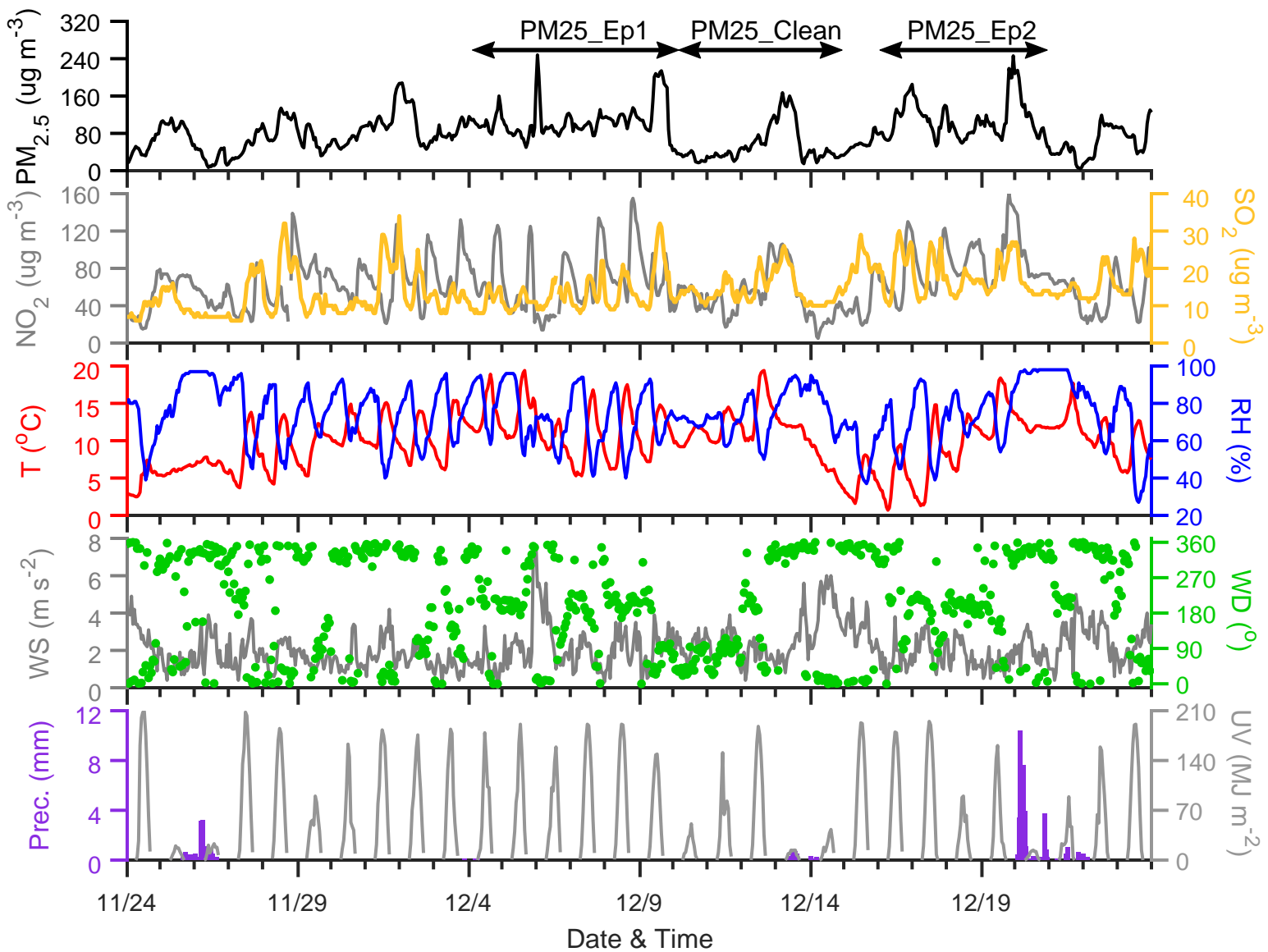


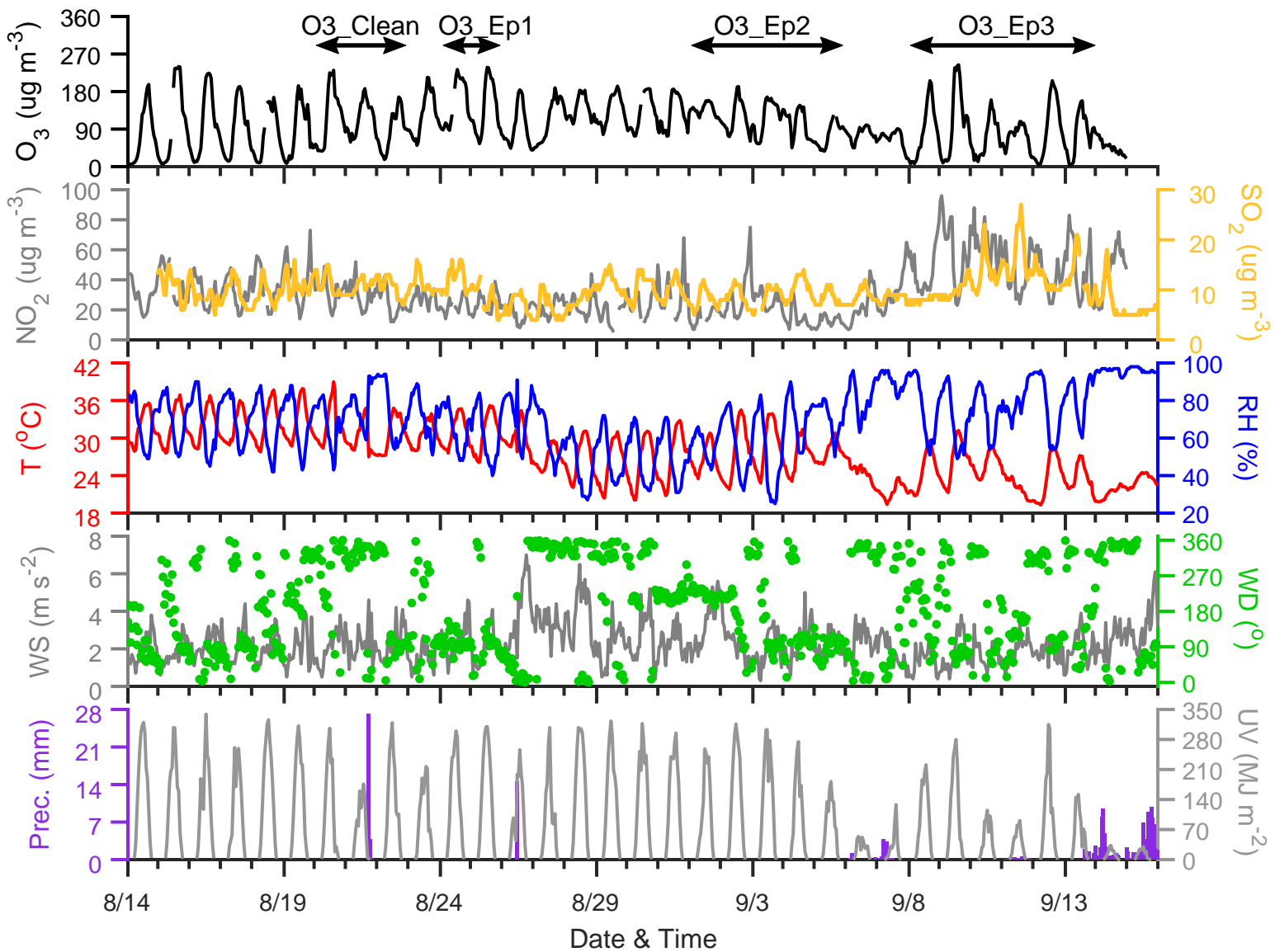


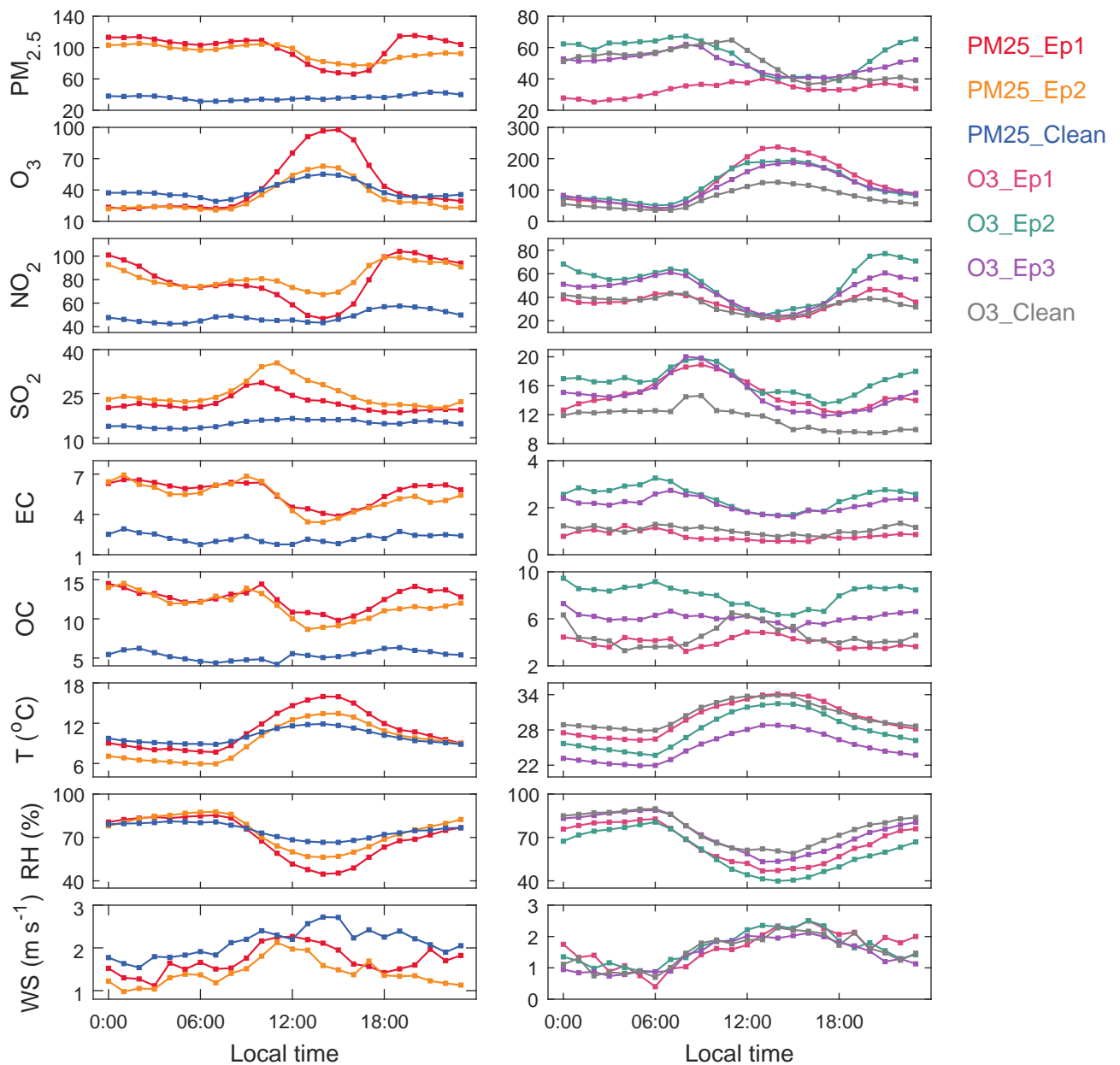


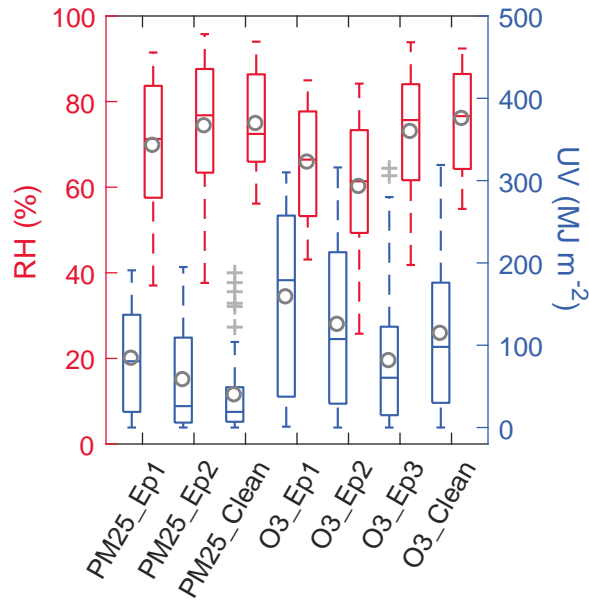
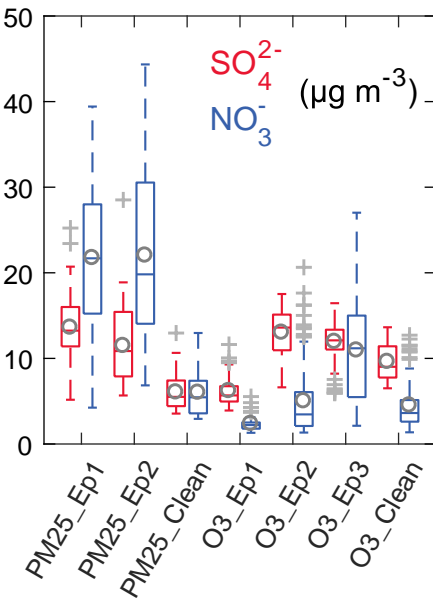
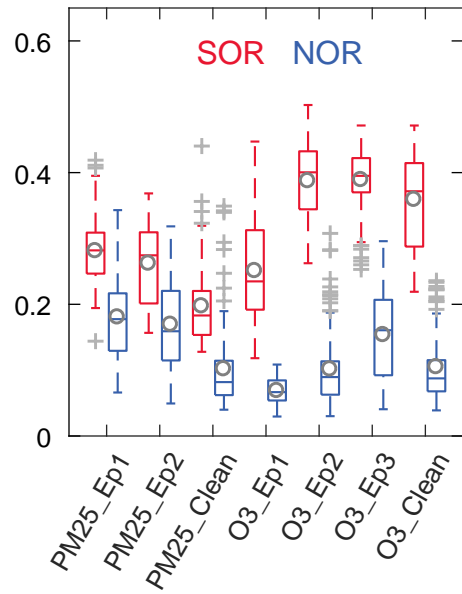












Episode

Highlights:

1. Regional severe PM_{2.5} and O₃ episodes over the YRD during a comprehensive field observation campaign (CAPUM-YRD) were characterized.
2. Particulate and ozone source apportionment technology were applied to explore the sources of PM_{2.5} and O₃.
3. Qualitative and quantitative contributions of different source regions to PM_{2.5} and O₃ in YRD were investigated.

ACCEPTED MANUSCRIPT

The authors declare that they have no actual or potential competing financial interests.

ACCEPTED MANUSCRIPT